

Pre-saccadic Rise Neurons In The Hindbrain Control The Timing Of Spontaneous Saccades

Authors/Affiliations

Alexandro D. Ramirez^{*1}

Emre R.F. Aksay¹

Correspondence

Alexandro D. Ramirez; alr2038@med.cornell.edu

Highlights

- Comprehensive analysis of cells involved in spontaneous saccades and fixations.
- Novel neuronal class with pre-saccadic rising activity that is predictive of saccade timing.
- Ablations in the pre-saccadic rise population lead to delayed saccades.
- New model system for understanding ramp-to-threshold dynamics and decision making.

¹ Department of Physiology and Biophysics; Weill Cornell Medicine; New York; New York; 10065

^{*}Lead Contact

Keywords: spontaneous movement, larval zebrafish, eye movements, calcium imaging

Abstract

The spontaneous generation of saccades and fixations provides a simple model for understanding how internal brain dynamics are linked to behavior. We coupled calcium imaging with focal laser ablations in larval zebrafish to comprehensively map the activity patterns underlying the generation and control of this spontaneous behavior. We found a continuum of activity types ranging from cells that burst only during saccades, to cells that displayed tonic discharge during fixations, to neurons whose activity rose in advance of saccades by multiple seconds before falling to baseline after saccade completion. The activity of these pre-saccadic rise neurons was predictive of upcoming saccade time when analyzed under the general framework of ramp-to-threshold models. Ablations in regions where these neurons were densest led to the greatest delay in saccade initiation. The rate of rise in these neurons was variable across cells and fixations, with increased slope coupled to shorter rise times. These findings suggest that the novel class of pre-saccadic rise neurons presented here are involved in the timing of self-initiated saccadic movements.

Introduction

The seemingly simple task of moving one's eyes to a location of interest and then fixating upon that location has offered neuroscientists a window onto numerous computations in the brain. For example, a beautiful representational transformation occurs in the encoding of visually-targeted, rapid eye movements, known as saccades. The superior colliculus (SC) encodes saccades of different amplitude and direction using a topographic map of movement fields (Gandhi and Katnani, 2011; Sparks, 2002). Activity on this map is transformed to a response in the brainstem saccadic burst generator, where saccade size is encoded by neuronal firing rate. This process thus constitutes a transformation from a place to a rate code. An important example of a dynamic signal transformation occurs when the burst signals from the saccade generator are integrated to form a tonic signal in the hindbrain Velocity-to-Position Neural Integrator. Recognition that the generation of fixation signals requires a temporal integration, and subsequent identification of brain regions composing the integrator (Baker and Berthoz, 1975), has led to a deeper understanding of the mechanisms of persistent neural activity in general (Cannon et al., 1983; Joshua and Lisberger, 2015; Pastor et al., 1994; Vishwanathan et al., 2017).

While much is known about the neural signal transformations involved in reflexive or visually-driven eye movements, much less is known about the neural signals and mechanisms underlying self-initiated eye movements. In the oculomotor system, a distributed network of activity involving the frontal eye fields and superior colliculus is necessary for making saccades after a visual target is presented (Schiller et al., 1979, 1980). Sensorimotor processing in this network translates target features into a saccadic command that is sent from the superior colliculus to the saccade burst generator in the reticular formation (Munoz et al., 2000; Scudder et al., 2002). In addition to these saccades to a presented target, numerous species also make completely spontaneous saccades (Easter, 1971; Wurtz and Goldberg, 1971), even in the dark or in the absence of specific visual cues. But where and what are the initiation signals triggering these spontaneous saccades when there is no sensory stimuli to transform into a movement signal? Lesion studies suggest that the planning and initiation of spontaneous saccades does not require the superior colliculus and forebrain circuits used for saccades to a specific visual target (Johnstone and Mark, 1969; Wurtz and Goldberg, 1972). One possibility is that neuronal populations in the extensive oculomotor circuitry of the hindbrain are responsible for the initiation and timing of spontaneous saccadic eye movements.

We used comprehensive optical mapping and targeted laser ablations to identify and analyze neuronal populations involved in the initiation of spontaneous saccades. We asked two main questions. Are there single-neurons in the hindbrain whose activity would support the initiation of spontaneous eye movements? And second, are these neurons necessary for the proper patterning of self-initiated eye movements? To address these questions, we imaged single-cell calcium activity from neurons throughout the hindbrain in larval zebrafish and performed focal laser ablations to test the functional role of the hindbrain in the initiation of spontaneous saccades. By 5 days post-fertilization, larval zebrafish exhibit spontaneous, alternating patterns of rapid eye movements and fixations similar to adult goldfish (Burrill and Easter, 1994; Easter, 1971). These eye movements are not reflexive responses to sensory input since, analogous to mammals (Mohler and Wurtz, 1976; Moschovakis et al., 1988; Wurtz and Goldberg, 1971), larval zebrafish can make spontaneous saccades in the dark, in the absence of sensory stimuli. This behavior can be elicited while the optically transparent animal is restrained (Miri et al., 2011), permitting large-scale imaging of calcium indicators at cellular resolution (Ahrens et al., 2012; Orger, 2016; Portugues et al., 2014) and targeted perturbations.

Our combined imaging and perturbation study provides three notable advances. One, we generated the first comprehensive map of hindbrain neuronal activity patterns underlying self-initiated saccades and subsequent fixations. Two, we found neurons in the hindbrain whose activity rises above baseline in a direction-selective manner multiple seconds before the decision to saccade. Furthermore, the time and rate of rise of these cells is consistent with a ramp-to-threshold model of spontaneous saccade initiation. Third, we found, through targeted ablations, evidence implicating these cells in controlling the proper patterning of spontaneous saccades. These findings not only provide insights into the mechanisms generating spontaneous eye movements, but also establish a new model system for understanding the neuronal processes underlying self-initiated movements and decision-making.

Results

In the first part of the results we present an analysis of spontaneous eye movements in the dark in larval zebrafish (Fig. 1) and a map of the average temporal dynamics of neurons sampled across the hindbrain that were active during this behavior (Fig. 2-3). We then analyze the temporal and spatial properties of a special class of neurons found in this map whose activity

suggests they play a role in eye movement initiation (Fig. 4-6). We end by systematically mapping how eye movement patterning is affected by bi-lateral lesions centered at different regions across the hindbrain (Fig. 7).

Larval zebrafish generate spontaneous eye movements with a range of inter-saccade times

Larval zebrafish reliably generated spontaneous eye movements consisting largely of a back-and-forth alternation of rapid eye movements known as saccades followed by longer periods of relatively constant eye position known as fixations (Fig. 1A, 2B). Spontaneous eye movements in the horizontal plane were measured in agar mounted larval zebrafish (7-8 days post fertilization) after releasing the eyes from the agarose (n=20; Fig. 1A). Experiments were performed in the dark to ensure that movements were self-initiated and not occurring in response to a visual target. Eye movements ranged over 2-28 degrees (1 and 99% quantiles), with a median amplitude of 12 degrees. The time between saccades was variable; fixations lasted between 2-50 seconds (1 and 99% quantiles) with a median duration of 11.4 seconds (Fig. 1B, 1C). To further examine the rhythmicity of these movements, we performed a Fourier analysis of the changes in eye position and found that power was distributed over a range of frequencies, with 95% of total power between 0-0.345 Hz, and peak power at 0.035 Hz (Fig. 1D). While there was a clear alternating cycle of leftward then rightward directed saccades (Fig. 1B), we found that it was not uncommon for eye movements to deviate from this simple pattern, as nearly a quarter of the time zebrafish made successive saccades in the same direction (22.9 \pm 0.3%, Fig. 1E). These results show that larval zebrafish can self-initiate a simple yet varying pattern of horizontal eye movements.

Mapping Activity Using Two-Photon Microscopy

To create a comprehensive map of the functional cell types involved in self-initiated eye movements, we imaged calcium dynamics throughout the larval zebrafish hindbrain (Fig. 2Ai, 2Aii) during spontaneously generated saccades and fixations in the dark. The seconds long fixation durations between eye movements (Fig. 1B, 1C) facilitated the use of calcium imaging to analyze changes in single-cell activity during fixations. Activity from neurons expressing nuclear-localized GCaMP6f under the control of the HuC pan-neuronal promoter was measured

with raster-scanning two-photon microscopy. The use of two-photon microscopy for imaging provided a high-signal to noise ratio (100 pixels per cell) and ease of single-neuron isolation (Fig. 2Aiii). In each fish ($n=20$), we imaged a portion of the hindbrain using a stack of 5-20 horizontal planes. Stacks from individual fish were then registered to a reference brain (Supplemental Fig. 1B, methods). The planes were centered at different rostral-caudal locations across fish so that when combined via registration we effectively sampled responses from the entire hindbrain, with each voxel sampled from at least 3 fish (Supplemental Fig. 1A, 1C)

We found that approximately a third of the neurons in the hindbrain showed some activity under these conditions. To measure how many cells were sampled in our data set, we used standard computer vision algorithms (methods) to infer the locations of all cell-nuclei based on time-averaged fluorescence intensity maps. We measured 280,959 cells from all planes and fish in our data set. This number is larger than the 120,000 neurons expected from sampling 3 complete hindbrains because some regions were sampled more than 3 times (Supplemental Fig. 1C). To infer the locations of active neurons, we performed a separate analysis using an algorithm that relies on non-negative matrix factorization (NMF) to distinguish non-responsive from responsive regions-of-interest (ROIs) (Pnevmatikakis et al., 2016). The NMF algorithm identified approximately 30% of hindbrain neurons (64,242 ROIs) as spontaneously active. As an additional check that the cells identified by the NMF algorithm were properly classified as active and non-active, we measured the maximal deviations in their fluorescence traces and compared this with the maximal deviations in fluorescence of cells classified as background. As expected, we found that cells identified by the NMF algorithm had greater deviations in fluorescence, on average, than cells classified as background (Supplemental Fig. 1D, 1E).

Neuronal Activity Dynamics Associated with Spontaneous Saccades and Fixations

Ten percent ($n=6,587$) of the spontaneously active hindbrain neurons had average activity related to eye movements. We aligned fluorescence responses from active cells to the times of spontaneous saccades and determined which neurons had significant saccade-triggered average (STA) activity. We treated individual fixations surrounding a saccade as single-trials (Fig. 2Bi-iii, methods) and performed a one-way ANOVA to compare the STA at different time bins to search for cells with significant deviations from baseline. Significant STAs had clear changes in dF/F around or at the time of saccade (Fig. 2Bi-iii). An analysis of each cell's STAs revealed a continuum of activity that ranged from cells with tonic activity during the post-

saccadic epoch (Fig. 2Bi), to cells that were only active at the time of saccade (Fig. 2Bii), to cells that were predominantly active during the pre-saccadic epoch (Fig. 2Biii).

We found a wide range of temporal dynamics across the population of cells. We used Principal Components Analysis to characterize the variations across STA profiles. We found that 93% of the variance in STAs could be explained by three principal components (Fig. 3A , first row). Each principal component (PC) had a temporal profile that varied notably at the time of saccade (Fig. 3A). We examined the distribution of principal component coefficients along the first three PCs to check if responses consisted of discrete or continuous combinations of the components (Fig. 3Bi). We normalized the coefficients so that all responses had the same unit magnitude, in order to focus on variations in profile shapes (Fig. 3Bii-iv). The PC coefficients for the population were broadly distributed (Fig. 3Biii-iv). The peaks in the density of coefficients corresponded to two distinctive STAs; one STA increased in dF/F following saccades while the other STA decreased (Fig. 3Biv). This pattern results from neurons selectively responding to either saccades to the left or saccades to the right. A K-means and Silhouette analysis of the combined left and right PC coefficients found that these data were best segregated by two clusters corresponding to left and right selectivity (Supplemental Fig. 2). Therefore, the Principal Components analysis uncovered a range of temporal dynamics in the population of STA responses that varied about a selective and non-selective direction.

The distribution of STA temporal dynamics across cells ranged from those that were sustained during a fixation, to those that burst during saccades, to those that rose gradually during the fixation and fell rapidly after the saccade. To characterize the temporal dynamics, we examined population averages of STAs grouped according to their normalized projections onto PCs 1 and 2 (the variable ϕ , ϕ , in Fig. 3Bii). The value of ϕ was kept constant, within 15 degrees, for each STA within a group (the 15 degree bin size was chosen so that each group contained at least 1% of the total cells related to eye movements). Before averaging, we deconvolved the STAs of these cells using a 2 second exponential kernel to approximate the effects of GCaMP6f calcium filtering on their average firing rate (Kawashima et al., 2016; Yaksi and Friedrich, 2006). Consistent with previous imaging and electrophysiological studies in the larval zebrafish and adult goldfish, we found populations of cells whose STAs have dynamics expected by velocity-to-position neural integrators and abducens motor neuron cells ($\phi = -45$ in Fig. 3C, Fig. 2Bi). These cells have pre-saccadic population activity that remained constant at baseline levels, rapidly increased to a peak response within a second (the temporal resolution of calcium

imaging) of the saccade time and then displayed tonic firing after the saccade. With increasing ϕ , we observed less sustained activity during fixations and more pronounced bursts of activity associated with the saccade, eventually reaching profiles similar to those reported for saccadic burst generator neurons ($\phi = 45$ in Fig. 3C, Fig. 2Bii). With larger ϕ , we see a pre-saccadic rise in activity that becomes longer in duration and more prominent relative to the burst event at the saccade ($\phi = 105$ in Fig. 3C, Fig. 2Biii). This pre-saccadic rise is suggestive of activity that anticipates saccades.

To reduce potential within-group variability about each population average bin, we subdivided cells within a group according to their projection along PC 3 and constructed population averages for each sub-group. We found that the qualitative trends in temporal dynamics described above remain largely unaffected by sub-dividing groups (Supplemental Fig. 3).

In summary, we found that about 3% of hindbrain neurons in larval zebrafish had responses associated with spontaneous saccades and fixations, these responses were direction-selective, and the response profile of this population was diverse. The diversity included cells with step-like profiles expected for abducens neurons and integrator neurons, and cells with burst-like responses expected for saccade generator neurons. The distribution also contained neurons whose activity is better described as anticipating upcoming movements, consistent with a role in motor preparation, a role which we explore below.

Single-Trial Analysis of Cells with Pre-Saccadic Rise Activity

Within the continuum described above were cells whose trial-average activity revealed an unusual form of firing rate dynamics, with activity that steadily rose ahead of the upcoming saccade. Because this form of dynamics appears to anticipate a future movement, it is reasonable to speculate that neurons with such activity play an important role in saccadic preparation or timing. We now turn our attention to a closer examination of such neurons, beginning with a single-trial analysis of cells with these dynamics.

We found that 6% ($n=424$) of eye-movement related hindbrain neurons had fluorescent activity that was positively correlated with time to upcoming saccade ($p<0.01$) (Fig. 4A). Here we note some of the key qualitative features of these neurons before providing detailed quantification. These cells showed clear increases in activity before individual saccades either to the left (Fig.

4A, neurons in 3rd and 4th row from top) or right (Fig. 4A, neurons in 1st and 2nd row from top). For each cell, pre-saccadic rise events ahead of saccades in one direction occurred very reliably, although there were rare occasions where cells failed to rise before a saccade towards the cell's selective direction (neuron in second row from top in Fig. 4A) or occasions where neurons rose before a saccade in the cell's non-selective direction (n=4 cells, not shown). Rise events generally lasted multiple seconds, and there was variability in the duration of the rise both within and across cells (Fig. 4A). Remarkably, for a given cell, activity rose to consistent values at the time of saccade, even though duration of rise varied by 50% or more. Finally, following a saccade in the ON direction, cell activity generally quickly returned to baseline. Because of these characteristics, we will refer to these cells as pre-saccadic rise (SR) neurons.

To quantitatively characterize the dynamics of SR cells, we assessed several features of their activity before and after saccades that could elucidate their role in initiating the upcoming spontaneous saccade (Fig. 4B, methods). In order to examine how the initiation of activity related to saccade occurrence, we measured the time when activity rose above baseline, and compared that to the time of upcoming and previous saccades (Fig. 4C-E). We also measured whether the time of activity rise scaled with fixation duration (Fig. 4F-G). To determine whether neuronal activity consistently rose to similar values, we measured activity at the time of saccade (Fig. 5F). Finally, to determine how quickly activity in these cells fell after saccades, we measured the time when their activity returned to baseline after a pre-saccadic rise event (Supplemental Fig. 4A).

The initiation of the rise event was more tightly coupled to the timing of the upcoming saccade rather than the timing of the previous saccade. Across cells and fixations, activity rose over a range of times between 2 and 10 seconds relative to the upcoming saccade (10 and 90% quantiles; median time = 5 seconds) (Fig. 4C). Across cells and fixations, the timing of activity initiation relative to the occurrence of the previous saccade was generally more variable, with a range of 1 to 13 seconds and variance that was 3 times larger than when measured with respect to upcoming saccade (Fig. 4D). Furthermore, we rejected the null hypothesis that these two measurements in the time of rise come from the same distribution (Fig. 4E, $p < 0.001$, $n = 4,146$; two-sample KS-test). A similar trend was observed when data was analyzed on a per cell basis: many cells had activity whose time of rise was more variable when measured relative to the previous saccade than when measured relative to upcoming saccade (Supplemental Fig.

4B). Therefore, the activity of SR neurons is more informative of upcoming saccades than previous saccades.

Given that there was notable variation in the time between saccades (Fig. 1C), we also tested for relationships between the time of rise and the duration of the fixation. To see if there was a constant scaling relationship between fixation duration and the time of SR activity rise, we examined the distribution of times of rise normalized by fixation duration. We found that, across cells and fixations, normalized rise times were not peaked at a single value, as expected if time of rise was linearly related to fixation duration, but rather non-uniformly distributed across the full range of possible values (Fig. 4F; $p < 0.001$, $n = 2,539$). The variability in normalized time of rise was related to fixation duration (Fig. 4G): there was a slight trend for activity to rise relatively quickly after the previous saccade during short fixation durations and for activity to rise later in the interval during longer fixations (Fig. 4G; best fit line slope = 0.012 ± 0.001 (1/s), offset = -0.647 ± 0.008). On a per cell basis, the time of normalized rise and fixation duration were only correlated for a small subset of SR neurons (less than 20%, Supplemental Fig. 4C, 4D); therefore the population trend reflects cell-to-cell differences. In summary, we found that SR cell activity can rise within any fraction of the fixation time, with a propensity, at the population level, to begin rising towards the latter half of a fixation.

Pre-Saccadic Rise Dynamics are Predictive of Upcoming Saccades

If SR cell activity determines when a spontaneous saccade should occur, we should be able to predict whether a saccade is about to happen based on the output of SR populations. Influential ramp-to-threshold models of saccade initiation to visual targets propose that saccades occur when single-neuron or population activity in the Superior Colliculus reaches a threshold level (Jantz et al., 2013) (Fig. 5A). Given that SR activity monotonically increases before saccades, we asked whether a threshold on SR population activity could be used to predict spontaneous saccade times. We calculated the population average activity of SR cells before an upcoming saccade in their preferred direction during different inter-saccade intervals. The population average activity reached similar levels at the time of saccade for different fixation durations (Fig. 5B). After determining an activity threshold for saccade initiation from a portion of the data used as a training set, we were able to predict the initiation of $63 \pm 1.6\%$ of the upcoming saccades from neural activity in a test data set (to within 2 seconds, or $\sim 18\%$ of the median fixation duration; methods). In contrast, when the same procedure was used for non-SR neurons, only

0.6 \pm 0.3% of the saccade times were predicted. Thus, pre-saccadic SR population activity can be used to predict when saccades will occur.

The relevance of the ramp-to-threshold model for understanding the mechanism by which spontaneous eye movements are initiated was also apparent at the single cell and single trial levels. For each cell and fixation, we measured the rate of activity change following the time when cell activity begins to rise. We approximated the growth in activity as linear, only using fixations where correlation between the data and model was greater than 0.7 (66% of fixations), and measured the slope of growth as a function of time (Fig. 5C). Across cells and fixations, the rate of rise in pre-saccadic activity varied between 0-60% (dF/F)/s (Fig. 5D). Furthermore, this variability in rate of rise was positively correlated with the time of pre-saccadic rise: slowly rising activity began to increase above baseline earlier than faster rising activity (Fig. 5E). At the individual cell level, this positive correlation was apparent for 45% of SR cells (Supplemental Fig. 4E, 4F). Finally, across cells and fixations, the relationship between the rate and time of rise was such that the average level of activity that these cells reached at the time of saccade was fairly constant (Fig. 5F, blue dots). We failed to reject the null hypothesis that the average level dF/F at the time of saccade varied with time of rise (for times < -3 ; $p=0.96$, F-test, $n=2,121$); this result held for all times when we deconvolved the data to remove the effects of calcium buffering (Fig. 5F, orange dots; $p=0.89$, F-test, $n=2,672$). In summary, we found that the rate of pre-saccadic rise in SR cells varies with the time of rise such that the population average reaches similar levels of activity, as expected by a threshold model of saccade initiation.

Spatial Distribution of Neurons with Pre-Saccadic Rise Dynamics

We next examined the spatial distribution across the hindbrain of cells with pre-saccadic rise dynamics. These neurons were broadly distributed across the rostral-caudal axis, with a small group in the cerebellum and rhombomere 1 (8%), the majority between rhombomeres 2-6 (71%), and a modest representation in rhombomeres 7-8 (21%) (Fig. 6A). SR neurons were more likely to be near the midline than near the edge of the brain (Fig. 6B). Along the dorsal-ventral axis, SR cells largely resided in a region that is 10-70 microns dorsal of the Mauthner cell (Fig. 6C). None of the SR cells were found in the abducens complex, consistent with previous literature on abducens firing rate properties (Pastor et al., 1991). Directional preference of pre-saccadic neurons was largely contraversive (Supplemental Fig. 5). The rostral-caudal

distribution of pre-saccadic neurons depended on the cell's position along the dorsal-ventral axis; the most ventral portions (10-40 microns above the Mauthner cell) contained nearly all the pre-saccadic neurons located in the caudal portion of the hindbrain (rhombomeres 7-8) (Fig. 6D).

Focal Laser Ablations Identify Hindbrain Regions Containing SR Cells as Indispensable for Determining Fixation Duration

In both fish and mammals it is unknown where the signals to initiate spontaneous saccade arise. The activity of the SR neurons we identified suggest that they initiate saccades when their population level activity reaches a threshold value. In the simplest instantiation of this model, activity is summed across cells and compared with a threshold value. If true, losses in the number of SR cells would lead to a longer time until saccades occur. To test this possibility, we performed bilateral two-photon laser ablations at different locations in the hindbrain where SR neurons are found and monitored changes in saccade and fixation metrics.

Given the broad rostral-caudal distribution of SR neurons (Fig. 6A), we made randomly targeted ablations across the hindbrain ($n = 32$ fish). Ablated regions were approximately cylindrical in shape with a diameter of 30 micrometers along the rostral-caudal and medial-lateral axis and a side-length of 60 microns along the dorsal-ventral axis (Fig. 7A; approximately 3% of the hindbrain). We first tested the effect of ablations on saccade velocity and the ability of animals to maintain fixation (Supplemental Fig. 6). We found no change in saccade velocity following hindbrain ablations. We did find a significant decrease in fixation stability following ablations in rhombomeres 7-8, consistent with previous literature (Miri et al., 2011), but did not see a significant decrease in fixation stability after ablations in regions rostral of rhombomeres 7-8.

We found that there was a significant increase in the fixation duration following ablations in the hindbrain (Fig. 7B,C). Given the broad rostral-caudal distribution of SR neurons (Fig. 6A), we made randomly targeted ablations across the hindbrain ($n = 32$ fish). We compared the distribution of fixation durations before and after ablations in the hindbrain with the distribution of fixation durations before and after ablations in the spinal cord, a region not likely involved in determining when to saccade (Fig. 7D). We rejected the null hypothesis that mean fixation durations across all conditions were equal (one-way ANOVA $p < 0.01$; $n = 8,278$ fixations before and 4,101 after from 23 fish with hindbrain ablations; $n = 911$ fixations before and 1,104

fixations after from 9 fish with spinal cord ablations) and we rejected the null hypothesis that the mean fixation duration before hindbrain ablations was equal to the mean fixation duration after ablations ($p < 0.01$ using a Bonferroni correction for multiple comparisons; mean durations equal 11.7 and 16.7 seconds before and after ablation respectively). However, we failed to reject the null hypothesis that the mean fixation duration was equal following spinal cord ablations (mean durations equal 13.8 and 13.4 seconds before and after respectively) suggesting that the increase in fixation duration after hindbrain ablation was not an artifact of global damage induced by the lesion. These results provide evidence for a hindbrain role in spontaneous saccade initiation.

To assess whether SR neurons are mediating the increase in fixation duration, we measured the increase in median fixation duration following ablation as a function of the estimated fraction of the SR population that was ablated. We took advantage of the fact that equal-size ablations made at different rostral-caudal locations will ablate different numbers of SR cells since this population was not uniformly distributed across the hindbrain. We found that the increase in fixation duration after ablation was positively correlated to the estimated fraction of SR cells within the ablated region (Fig. 7E; $cc=0.74$, F-test p -value < 0.01 ; $n=13$ points from 23 fish). We also measured the increase in fixation duration after ablation as a function of the estimated fraction of non-SR cells ablated for each animal (Fig. 7F). We found that despite the overlapping distribution of SR and non-SR cells along the rostral-caudal axis (Fig. 6A, Supplemental Fig. 7), the increase in median fixation duration was not correlated with the number of non-SR cells ablated ($cc=0.30$, F-test p -value=0.32; $n=13$ points from 23 fish). Thus, these results suggest that loss of SR cells selectively disrupts the timing of saccades.

Discussion

We combined focal laser ablations and calcium imaging to comprehensively map neuronal function and activity during a self-initiated behavior. We simultaneously measured eye movements and neuronal activity throughout the hindbrain of larval zebrafish while they made spontaneous saccades in the dark. We discovered neurons in the hindbrain whose activity rises above baseline in a direction-selective manner multiple seconds before the occurrence of a saccade. We also implicated, through targeted ablations, a causal role for these cells in the decision to perform a spontaneous saccade. These data thus help elucidate the mechanism of a simple self-initiated decision.

A great number of animal movements are initiated in the absence any immediate external cue. Are there common underlying causes and dynamics that trigger self-initiated actions? The seconds long build in activity shown by SR cells is a prime candidate. Prior work has found similar neural activity ahead of seemingly voluntary walking in crayfish (Kagaya and Takahata, 2010, 2011), arm movements in non-human primates (Maimon and Assad, 2006), and limb movements in humans (Kornhuber and Deecke, 1965; Matsushashi and Hallett, 2008; Schurger et al., 2012). Our findings add to the evidence that this ramp-like dynamic is a common, internally-generated ‘readiness’ signal because our data were acquired in the complete absence of visual cues. Furthermore, our comprehensive mapping of this signal facilitated targeted ablations that showed a causal relationship between the degree of disruption to the readiness signal and delays in the initiation of saccades. Our work thus builds upon prior studies of signaling during voluntary movements by drawing a direct link between readiness signals and self-initiated movement.

The activity of SR neurons is consistent with that expected by a drift-diffusion model for triggering behavior. In these models, an internal signal is accumulated in value until a threshold is reached, at which point a command is given to trigger movement. While typically applied to psychophysics experiments, where the internal signal represents evidence for a task-relevant decision (Churchland and Kiani, 2016; Hanes and Schall, 1996; O’Connell et al., 2018), the general features of such ‘ramp-to-threshold’ models are also applicable here. We found that regardless of the duration of the readiness signal, the activity reached a fairly constant value at the time saccades were initiated (Fig. 5), suggesting a readiness threshold had to be crossed to trigger the saccade. Future studies that transiently manipulate SR neuron activity while monitoring behavior should help test the details of this hypothesis.

Our comprehensive assessment of hindbrain signaling during spontaneous saccades and fixations help constrain the set of network mechanisms which may explain the dynamics of SR neurons. We found a continuum of eye movement-related signaling types present in the hindbrain, with SR neurons firing in advance of a minority of cells that carried a saccadic burst signal and a majority with burst-tonic or more tonic firing during the fixation. A similar spectrum of coding properties was also observed in recent work looking at zebrafish eye movements during phototaxis (Wolf et al., 2017), making it unlikely that we missed any prominent signaling motifs. How might the activity of SR neurons be linked to that of the other types in the continuum? At the time that SR neurons are ramping, the majority of the activity in the hindbrain

is that of the tonic neurons with opposing directional preference and little relaxation in activity. Therefore, one interesting possibility is that the ongoing fixation related activity in regions outside of the caudal hindbrain, where ablations led to a fixation deficit consistent with a loss of neural integration, could provide a kind of evidence signal that SR neurons accumulate.

Understanding the circuit and cellular mechanisms underlying the seemingly universal ramping signal will require a combination of anatomy, perturbation experiments, electrophysiology and mathematical modeling. One key advantage of discovering the SR signal in larval zebrafish is that in this animal one has the ability to image and manipulate single cells across the entire brain (dal Maschio et al., 2017; Vanwalleghem et al., 2018) and perform whole-circuit connectomics analysis in functionally-specified populations (Vishwanathan et al., 2017). These tools are important for accurately determining synaptic contributions to the pre-movement signal. The mechanistic insights that one can obtain on readiness in larval zebrafish will hopefully allow us to understand a broad set of decision-making processes.

Author Contributions

A.D.R. and E.R.F.A. conceived the project; A.D.R. carried out the experiments and analyzed the data; A.D.R. and E.R.F.A. wrote the paper.

Acknowledgements

We thank Chao Young and Misha Ahrens for generating the Tg(HuC:GCaMP6f-H2B) line and sharing ahead of publication. We thank RARC team at Weill Cornell Medicine for animal husbandry. We thank Misha Ahrens, Ari Arrenberg, Robert Baker, Tom Chartrand, Charlotte Grove, Mark Goldman, and Gaby Maimon for helpful discussion and feedback on the manuscript. Funding for this work was provided by NIH grant K99 EY027017, R01 EY021581 and the Simons Foundation Global Brain Initiative.

Materials and Methods

Calcium Imaging and Eye Tracking

All experimental procedures were approved by Weill Cornell Medicine's Institutional Animal Care and Use Committee. Transgenic larvae (7-8 days post-fertilization) expressing nuclear-localized GCaMP6f, Tg(HuC:GCaMP6f-H2B; strain cy73-431), were kindly provided by Misha Ahrens' lab. Fish were embedded in 1.5% low-temperature agarose and subsequently imaged using a custom-built two-photon laser scanning microscope (Daie, Goldman, & Aksay, 2015) that was controlled using ScanImage v3.5 in Matlab 2007 (Pologruto et al., 2003). We performed two-photon imaging using excitation light (930 nanometers) from a tunable laser (Spectra-Physics Mai Tai) sent through a 40x (0.8 NA) water-immersion objective lens (Olympus LUMPLFL40XW/IR2) to the hindbrain. The laser power was controlled using an electro-optical modulator (Conoptics 350-50UV) and amplifier (Conoptics 302RM). Laser power used for imaging ranged from 15-25 mW at the sample. Neurons within square horizontal planes (185 microns in length; 5-20 planes per fish spaced apart by 5 microns) were imaged simultaneously at 0.98 Hz (512 lines at 2 milliseconds per line). Recordings lasted 4-5 minutes per plane. Images were saved as uncompressed grayscale TIFF stacks. Horizontal eye movements were tracked in real time using a sub-stage CMOS camera (Allied Vision Technologies, Guppy FireWire camera) illuminated with infra-red light (850nm, Thorlabs 851L). Custom Matlab software extracted horizontal eye position (e in Fig. 1A) from camera images in real-time at a variable sampling rate of approximately 13 Hz based on an algorithm described in (Beck et al., 2004; Miri et al., 2011). Eye position traces were stored as MAT files (Matlab).

Automated Identification of Regions of Interest

Prior to analysis, each calcium movie was pre-processed to correct for motion artifacts (see Supplemental Procedures for details).

Finding the Locations of all Cell Nuclei Based on Time-Averaged Images

For each motion-corrected fluorescence movie, we calculated the median intensity across time for each pixel and analyzed the resulting time-averaged image to find individual cell nuclei locations. We performed a morphological opening on the time-averaged image (Matlab function *imopen*) with a disk-shaped structuring element that had a radius equal to 4 pixels (1.4

microns). The opening operation with this structuring element tended to make it easier to segregate the disk-shaped nuclei in the image. We then found local intensity maxima of the opened image by looking for connected pixels with equal intensity that were greater than the intensity of external boundary pixels (Matlab function *imregionalmax*). We measured the locations of individual cell nuclei measuring the regions of connected pixels that corresponded to local intensity maxima. To control for false positives, we excluded any selected ROIs that had an area greater than 144 pixels squared (19 microns squared).

Finding the Locations of all Cell Nuclei Based on Fluorescence Dynamics

We implemented the alternating matrix factorization framework described in detail in (Pnevmatikakis et al., 2016) on motion-corrected fluorescence movies using the freely available CalmAn-MATLAB matlab toolbox provided by the Flatiron Institute (<https://github.com/flatironinstitute/CalmAn-MATLAB>). When determining the location of active neurons, we only used estimates of the spatial components provided by the algorithm. The toolbox allowed for flexibility in the initialization procedures and in the ordering and number of alternating factorizations. We implemented a procedure based on the 'demo_script.m' file provided with the code. After initializing the spatial and temporal components with a greedy procedure, we ran 1 iteration of spatial and temporal updates, followed by a post-processing step where similar components were merged and unrealistically large components were removed, followed by a final spatial and temporal update. We investigated different values of the number of neurons parameter, K, and chose a value (250) that produced reasonable looking spatial footprint estimates based on visual inspection of a handful of sample fluorescence movies. Unless stated otherwise, subsequent analysis only relied on the fluorescence trace found by spatially-averaging across pixels within the final spatial footprints found by this NMF-based algorithm (see Supplemental Procedures for more details on the CalmAn-MATLAB routines used).

Automated Determination of Saccade Times

We determined the times of saccade occurrence by calculating the crossing times of eye velocity past a threshold. To calculate eye velocity, we filtered eye position using a median filter (medfilt1 in Matlab 9.2.05). The exact value of the filter order depended on the eye position sampling rate but was chosen to correspond to 500 milliseconds. We approximated eye velocity

as the difference in filtered eye position at consecutive time points divided by the time difference between these points. The threshold was set to three standard deviations above the mean absolute velocity or 10 degrees per second, whichever was larger. A single saccadic event typically consisted of several consecutive points whose instantaneous velocity was above the threshold. We took the initial point as the time when the saccade occurs.

Saccade-Triggered Average (STA) Calculation

We averaged saccade-triggered signals across fixations after interpolating them to a grid of time points equally spaced apart by 1/3 seconds. dF/F was computed as $(F-F_0) / F_0$ where F is the average fluorescence within a cell's ROI and F_0 is the mean fluorescence across the entire recording period. dF/F before and after each saccade was extracted and linearly interpolated to a grid of time points equally spaced apart by 1/3 seconds. Saccade-triggered signals were then grouped according to the direction of saccade (left or right). 95% confidence intervals about the average (Fig. 2B) were found by resampling the saccade-triggered responses with replacement and calculating the STA for each resample (number of resamples = 100). We measured the lower and upper bounds of the confidence intervals as the 2.5% and 97.5% quantiles across the bootstrapped samples. Since individual fixations ranged from 2-60 seconds, the number of trials available to construct the STA was a decreasing function of time from saccade and varied across experiments. Therefore, to compare STAs from different planes and different fish for the PCA analysis we needed to choose a fixed window surrounding the saccade. We computed the STA in a window that extended 5 seconds before and after saccade and only analyzed imaging planes where the animal made at least 5 saccades in both directions.

Selection of Cells Related to Eye Movements

We used a One-Way ANOVA (Matlab 9.2.05 function *anova1*, 'Statistics and Machine Learning Toolbox') to test the null hypothesis that STA activity at all timepoints was equal versus the alternative that at least one timepoint had average activity that differed from the others. We considered a neuron as being eye movement-related if we rejected the null hypothesis for either one of that neuron's STAs (either triggered around saccades to the left or right). We excluded any cells that were recorded during an experiment that contained less than 5 saccade-triggered

responses, around either saccades to the left or right. Each response was required to last at least 5 seconds before and after saccade. We used the Holm-Bonferroni method (Holm, 1979) to correct for multiple comparisons. This procedure varied the significance level for each comparison using the formula $p/(N - j + 1)$, where j was the index of the comparison after sorting p-values from low to high, p was the desired family-wise error rate, and N was the total number of comparisons. We set p to 0.01 and set the number of comparisons to $59,274 \times 2 = 118,548$, which was the total number of ROIs found by the NMF algorithm (after removing cells with too few trials) times two to account for both left and right trials.

Distinguishing SR Cells from Non-SR cells

We calculated the correlation coefficient between the time until an upcoming saccade and dF/F before each saccade using Spearman's rho (Matlab 9.2.05 'Statistics and Machine Learning Toolbox' function *corr* with option 'type' set to 'Spearman'). The Spearman correlation can be used to measure monotonic, not only linear, relationships between two variables X and Y . It is calculated as the standard Pearson correlation coefficient applied to the ranks of X and Y . We did not interpolate fluorescence activity before computing the correlation coefficient. We measured a correlation coefficient for each eye movement-related cell. We computed a p-value for each correlation coefficient by testing the hypothesis that $\rho = 0$ against the alternative that the correlation was greater than 0 ('tail' option set to 'right'). A neuron was considered to have significant pre-saccadic activity if we rejected the null hypothesis before either leftward or rightward directed saccades at a significance level of 0.01. We used the Holm-Bonferroni method to correct for multiple comparisons. Since each of our correlation calculations used more than 10 samples, the *corr* function used large-sample approximations of the expected distribution under the null hypothesis. The approximation relied on either the Central Limit Theorem (when the data had ties) or on a power series expansion in $1/n$ of the upper tail probability of ρ , where n was the number of samples (Best and Roberts, 1975).

Measuring Time and Rate of Pre-Saccadic Rise and Fall

Measuring Time of Pre-Saccadic Rise and Fall

We estimated the timing of pre and post-saccadic activity in SR cells by first constructing non-negative, deconvolved estimates of their firing rate by re-running the *update_temporal_components* function provided by the CalmAn-MATLAB matlab toolbox (see methods section *Automated Identification of Regions of Interest*). For each SR cell, we re-ran *update_temporal_components* using an auto-regressive parameter equal to 1 (note that this parameter value is different than the value of zero originally used to find the SR location). The function *update_temporal_components* provided estimates of denoised fluorescence activity and non-negative spike estimates given spatial components and a background signal. We re-ran the algorithm using the spatial components of SR cells found by our original run of the alternating matrix factorizations procedure as described in methods section *Automated Identification of Regions of Interest*. As an estimate of the spatial background component we used the image formed by first averaging fluorescence changes across time and then setting the locations of SR cells to zero. We used the average across all pixels as the temporal background component. As described in the documentation, *update_temporal_components* ran a block-coordinate descent algorithm (we used 2 iterations), which deconvolved the activity of each SR cell after removing the effect of all the other SR cells. We used the default 'constrained_foopsi' method along with the CVX toolbox for deconvolution, which solved a noise-constrained optimization problem to produce estimates of denoised fluorescence activity and non-negative spike estimates. The noise level for each neuron was estimated by averaging the power spectral density of component fluorescence activity with time over "high" frequencies (one half the Nyquist frequency to the Nyquist frequency which equaled 0.24-0.49 Hz for our data). We fixed the auto-regressive time constant to 1.8 seconds (in the equivalent continuous-time model) which roughly corresponded to the calcium buffering time for nuclear-localized GCaMP6f (Kawashima et al., 2016).

We analyzed the non-negative, deconvolved estimates of each SR cell's firing rate to determine pre and post-saccadic event times. We found, upon visual inspection of SR fluorescence traces, that we could reasonably distinguish times when a signal was active from non-active times by determining when SR firing rates crossed a threshold close to zero (0.1). We measured the time of pre-saccadic rise as the time before upcoming saccade when SR firing rate increased above threshold. We measured the time when activity returned to baseline as the time when SR firing rate returned below threshold. In some cases, the firing rate estimate had a discontinuous shape while the fluorescence activity was clearly continuous. In these cases, the firing rate was above threshold for several seconds, then below threshold for 1-2 samples (1.02-2.05 seconds),

then above threshold for several seconds. We did not count these events as part of the start and stop times.

Measuring Rate of Pre-Saccadic Rise

We estimated the rate of pre-saccadic rise by finding the slope of the best fit line of a segment of SR fluorescence activity with time. To construct the best fit line we used fluorescence values that occurred within a window from 1.1 seconds (1-2 samples) before the measured time of pre-saccadic rise to the time of the upcoming saccade.

Predicting Saccade Times Based on Pre-Saccadic Activity

We used a threshold model on population average, SR cell activity to predict when saccades occurred. For every SR neuron, dF/F before each saccade was linearly interpolated to a grid of equally spaced time points (1/3 second bins) starting from the previous saccade. We grouped these segmented dF/F values across all cells according to the accompanying fixation duration (time since previous saccade), using non-overlapping duration values equal to 2.5 +/- 0.5, 3.5 +/- 0.5, ..., 20.5 +/- 0.5 seconds. We randomly assigned 50% of the segments in each group to a “training” set, which was used to calculate the threshold. The threshold was calculated as the population average, interpolated dF/F at the time of saccade. For each of the remaining fixations (the “test” set), we predicted the time of upcoming saccade (the time when the population average crossed threshold) and compared this value with the actual time of upcoming saccade. We scored a saccade as incorrectly predicted if the threshold was never crossed within the duration or if the predicted time was earlier than the actual time by 2 seconds. Note that if the population average would have crossed the threshold within 2 seconds after the actual saccade time, our score would still have marked the trial as incorrectly predicted. We used this scoring procedure to determine the number of correctly predicted saccades across all fixation durations in the test set. By varying the randomly chosen samples that were used in training and testing sets we were able to score 950 trials. The value of the probability that we reported in the text of correctly determining saccade times, was calculated using the mean and standard error in the number of correctly predicted saccades out of these 950 trials.

Registration of Individual Planes to a Reference Brain

Each imaging plane was registered to a corresponding plane in a reference brain constructed from a single Tg(HuC:H2B-GCaMP6f) fish (8 dpf). We used common features such as fiber bundles, the midline, and ventricles found across larval zebrafish brains to select matching points with the reference brain. We registered each plane using an affine transformation uniquely constructed for that plane based on the hand selected match points. The linear affine transformation matrix was calculated using Matlab's *fitgeotrans* algorithm with the *transformationType* option set to affine. The algorithm used linear regression to estimate the affine transformation matrix based on the user-selected control points. To construct the reference brain, we stitched together six overlapping 512x512 (185 micron squared area) images to form a single plane in the reference brain. Each image used in the stitching procedure was formed by averaging calcium activity over a 20 second interval. The six images used were sufficient to completely tile any horizontal plane in the hindbrain. Images were taken from planes (spaced apart by 3 microns in the dorsal-ventral axis) that extended from the most dorsal portion of the hindbrain to the most ventral portion where expression was no longer visible. When we examined the quality of registration to the reference brain (Supplemental Fig. 1B), we found that qualitatively similar accuracies in registration could be achieved within neighboring dorsal-ventral planes (± 6 microns).

Laser Ablations

Ablations were performed with the same microscope used for imaging by implementing the procedure described in (Miri et al., 2011). We targeted regions along the dorsal-ventral axis that were 30 microns dorsal of the medial longitudinal fasciculus since this is where we found the majority of eye movement-related cells. Localized ablations were created by focusing the laser to an area smaller than a single cell and then increasing the average laser power to high values (130-150 mW) for 1-5 seconds. We repeated this procedure until we saw a lesion, which we determined by looking for a multi-spectrum spot that was much brighter than the fluorescence of surrounding tissue. Lesion sizes with this procedure were generally around 5 microns in diameter. To increase the size of the lesion we lowered the average laser power to values of 30-50 mW and imaged the ablated region which caused the lesion size to grow. We stopped imaging the ablated region once it was approximately 30 microns in diameter. We waited

between 30-120 minutes after ablation before recording post-lesion eye-movements. Post-lesions eye movements were recorded over a period between 10-30 minutes.

Analysis of Laser Ablated Regions

We took time-averaged images (minimum of 8 frames) of each ablated region. To approximate the location of the ablation damage center, we manually inspected each image and recorded the location of the bright, multi-spectrum fluorescence characterizing ablation. To compare ablation locations across animals in Fig. 7E, Fig. 7F, and Supplemental Fig. 7, we registered each image to our reference brain in the same way as described in methods sections *Registration of Individual Planes to a Reference Brain*. To estimate the fraction of SR cells lesioned in a given fish, we calculated the number, n_c , of SR cells (after registering their locations to the reference brain) that fell within a cylinder (30 micron radius, 60 micron side length along dorsal-ventral axis) centered at the registered lesion location. The fraction ablated was equal to n_c divided by the total number of SR cells. We repeated this procedure for non-SR cells. To reduce variability across animals in Fig. 7E and Fig. 7F, we averaged together individual estimates of fraction ablated from animals that were lesioned in similar regions. Specifically, we created an equally spaced grid (spacing equal to ablation radius of 30 microns) between the minimum and maximum registered lesion locations. Values of fraction ablated and fractional increase in fixation duration from animals whose lesion locations were registered to the same bin were averaged together to form an individual dot in Fig. 7E and Fig. 7F.

For more details regarding imaging analyses and statistics see Supplemental Experimental Procedures.

References

- Ahrens, M.B., Li, J.M., Orger, M.B., Robson, D.N., Schier, A.F., Engert, F., and Portugues, R. (2012). Brain-wide neuronal dynamics during motor adaptation in zebrafish. *Nature* 485, 471–477.
- Baker, R., and Berthoz, A. (1975). Is the prepositus hypoglossi nucleus the source of another vestibulo-ocular pathway? *Brain Res.* 86, 121–127.
- Beck, J.C., Gilland, E., Baker, R., and Tank, D.W. (2004). Instrumentation for measuring oculomotor performance and plasticity in larval organisms. *Methods Cell Biol.* 76, 385–413.
- Best, D.J., and Roberts, D.E. (1975). Algorithm AS 89: The Upper Tail Probabilities of Spearman's Rho. *J. R. Stat. Soc. Ser. C(Appl. Stat.)* 24, 377–379.
- Burrill, J.D., and Easter, S.S. (1994). Development of the Retinofugal Projections in the Embryonic and Larval Zebrafish (*Brachydanio rerio*). *J. Comp. Neurol.* 346, 583–600.
- Cannon, S.C., Robinson, D.A., and Shamma, S. (1983). A Proposed Neural Network for The Integrator of the Oculomotor System. *Biol. Cyberkinetics* 49, 127–136.
- Churchland, A.K., and Kiani, R. (2016). Three challenges for connecting model to mechanism in decision-making. *Curr. Opin. Behav. Sci.* 11, 74–80.
- Daie, K., Goldman, M.S., and Aksay, E.R.F. (2015). Spatial Patterns of Persistent Neural Activity Vary with the Behavioral Context of Short-Term Memory. *Neuron* 85, 847–860.
- dal Maschio, M., Donovan, J.C., Helmbrecht, T.O., and Baier, H. (2017). Linking Neurons to Network Function and Behavior by Two-Photon Holographic Optogenetics and Volumetric Imaging. *Neuron* 94, 774–789.
- Easter, S.S. (1971). Spontaneous eye movements in restrained goldfish. *Vision Res.* 11, 333–342.
- Gandhi, N.J., and Katnani, H.A. (2011). Motor Functions of the Superior Colliculus. *Annu. Rev. Neurosci.* 34, 205–231.
- Guizar-Sicairos, M., Thurman, S.T., and Fienup, J.R. (2008). Efficient subpixel image registration algorithms. *Opt. Lett.* 33, 156–158.
- Hanes, D.P., and Schall, J.D. (1996). Neural control of voluntary movement initiation. *Science* 274, 427–430.
- Holm, S. (1979). A Simple Sequentially Rejective Multiple Test Procedure. *Scand. J. Stat.* 6, 65–70.
- Jantz, J.J., Watanabe, M., Everling, S., and Munoz, D.P. (2013). Threshold mechanism for saccade initiation in frontal eye field and superior colliculus. *J. Neurophysiol.* 109, 2767–2780.
- Johnstone, J., and Mark, R.. (1969). Evidence for efference copy for eye movements in fish. *Comp. Biochem. Physiol.* 30, 931–939.
- Joshua, M., and Lisberger, S.G. (2015). A tale of two species: Neural integration in zebrafish and monkeys. *Neuroscience* 296, 80–91.
- Kagaya, K., and Takahata, M. (2010). Readiness discharge for spontaneous initiation of walking in crayfish. *J. Neurosci.* 30, 1348–1362.
- Kagaya, K., and Takahata, M. (2011). Sequential Synaptic Excitation and Inhibition Shapes Readiness Discharge for Voluntary Behavior. *Science* 332, 365–368.
- Kawashima, T., Zwart, M.F., Yang, C.T., Mensh, B.D., and Ahrens, M.B. (2016). The Serotonergic System Tracks the Outcomes of Actions to Mediate Short-Term Motor Learning. *Cell* 167, 933–946.

- Kornhuber, H.H., and Deecke, L. (1965). Hirnpotentialänderungen bei Willkürbewegungen und passiven Bewegungen des Menschen: Bereitschaftspotential und reafferente Potentiale. *Pflugers Arch. Gesamte Physiol. Menschen Tiere* 284, 1–17.
- Maimon, G., and Assad, J.A. (2006). Parietal area 5 and the initiation of self-timed movements versus simple reactions. *J. Neurosci.* 26, 2487–2498.
- Matsushashi, M., and Hallett, M. (2008). The timing of the conscious intention to move. *Eur. J. Neurosci.* 28, 2344–2351.
- Miri, A., Daie, K., Burdine, R.D., Aksay, E., and Tank, D.W. (2011). Regression-Based Identification of Behavior-Encoding Neurons During Large-Scale Optical Imaging of Neural Activity at Cellular Resolution. *J. Neurophysiol.* 105, 964–980.
- Mohler, C.W., and Wurtz, R.H. (1976). Organization of monkey superior colliculus: intermediate layer cells discharging before eye movements. *J. Neurophysiol.* 39, 722–44.
- Moschovakis, A.K., Karabelas, A.B., and Highstein, S.M. (1988). Structure-function relationships in the primate superior colliculus. II. Morphological identity of presaccadic neurons. *J. Neurophysiol.* 60, 263–302.
- Munoz, D.P., Dorris, M.C., Pare, M., and Everling, S. (2000). On your mark, get set: brainstem circuitry underlying saccadic initiation. *Can J Physiol Pharmacol* 78, 934–944.
- O’Connell, R.G., Shadlen, M.N., Wong-Lin, K., and Kelly, S.P. (2018). Bridging Neural and Computational Viewpoints on Perceptual Decision-Making. *Trends Neurosci.*
- Orger, M.B. (2016). The Cellular Organization of Zebrafish Visuomotor Circuits. *Curr. Biol.* 26, R377–R385.
- Pastor, A.M., Torres, B., Delgado-Garcia, J.M., and Baker, R. (1991). Discharge characteristics of medial rectus and abducens motoneurons in the goldfish. *J. Neurophysiol.* 66, 2125–2140.
- Pastor, A.M., De la cruz, R., and Baker, R. (1994). Eye Position and Eye Velocity Integrators Reside in Separate Brainstem Nuclei. *Proc. Natl. Acad. Sci.* 91, 807–811.
- Pnevmatikakis, E.A., Soudry, D., Gao, Y., Machado, T.A., Merel, J., Pfau, D., Reardon, T., Mu, Y., Lacefield, C., Yang, W., et al. (2016). Simultaneous Denoising, Deconvolution, and Demixing of Calcium Imaging Data. *Neuron* 89, 285–299.
- Pologruto, T.A., Sabatini, B.L., and Svoboda, K. (2003). ScanImage: flexible software for operating laser scanning microscopes. *Biomed. Eng. Online* 2, 13.
- Portugues, R., Feierstein, C.E., Engert, F., and Orger, M.B. (2014). Whole-Brain Activity Maps Reveal Stereotyped, Distributed Networks for Visuomotor Behavior. *Neuron* 81, 1328–1343.
- Schiller, P.H., True, S.D., and Conway, J.L. (1979). Effects of frontal eye field and superior colliculus ablations on eye movements. *Science* 206, 590–592.
- Schiller, P.H., True, S.D., and Conway, J.L. (1980). Deficits in eye movements following frontal eye-field and superior colliculus ablations. *J Neurophysiol* 44, 1175–1189.
- Schurger, A., Sitt, J.D., and Dehaene, S. (2012). An accumulator model for spontaneous neural activity prior to self-initiated movement. *Proc. Natl. Acad. Sci. U. S. A.* 109, E2904-13.
- Scudder, C., Kaneko, C., and Fuchs, A.F. (2002). The brainstem burst generator for saccadic eye movements: a modern synthesis. *Exp. Brain Res.* 142, 439–462.
- Sparks, D.L. (2002). The brainstem control of saccadic eye movements. *Nat. Rev. Neurosci.* 3, 952–964.

- Vanwalleghe, G.C., Ahrens, M.B., and Scott, E.K. (2018). Integrative whole-brain neuroscience in larval zebrafish. *Curr. Opin. Neurobiol.* 50, 136–145.
- Vishwanathan, A., Daie, K., Ramirez, A.D., Lichtman, J.W., Aksay, E.R.F., and Seung, H.S. (2017). Electron Microscopic Reconstruction of Functionally Identified Cells in a Neural Integrator. *Curr. Biol.* 27, 2137–2147.
- Wolf, S., Dubreuil, A.M., Bertoni, T., Böhm, U.L., Bormuth, V., Candelier, R., Karpenko, S., Hildebrand, D.G.C., Bianco, I.H., Monasson, R., et al. (2017). Sensorimotor computation underlying phototaxis in zebrafish. *Nat. Commun.* 8, 1–12.
- Wurtz, R.H., and Goldberg, M.E. (1971). Superior colliculus cell responses related to eye movements in awake monkeys. *Science* 171, 82–84.
- Wurtz, R.H., and Goldberg, M.E. (1972). Activity of superior colliculus in behaving monkey. IV. Effects of lesions on eye movements. *J. Neurophysiol.* 35, 587–596.
- Yaksi, E., and Friedrich, R.W. (2006). Reconstruction of firing rate changes across neuronal populations by temporally deconvolved Ca²⁺ imaging. *Nat Methods* 3, 377–383.

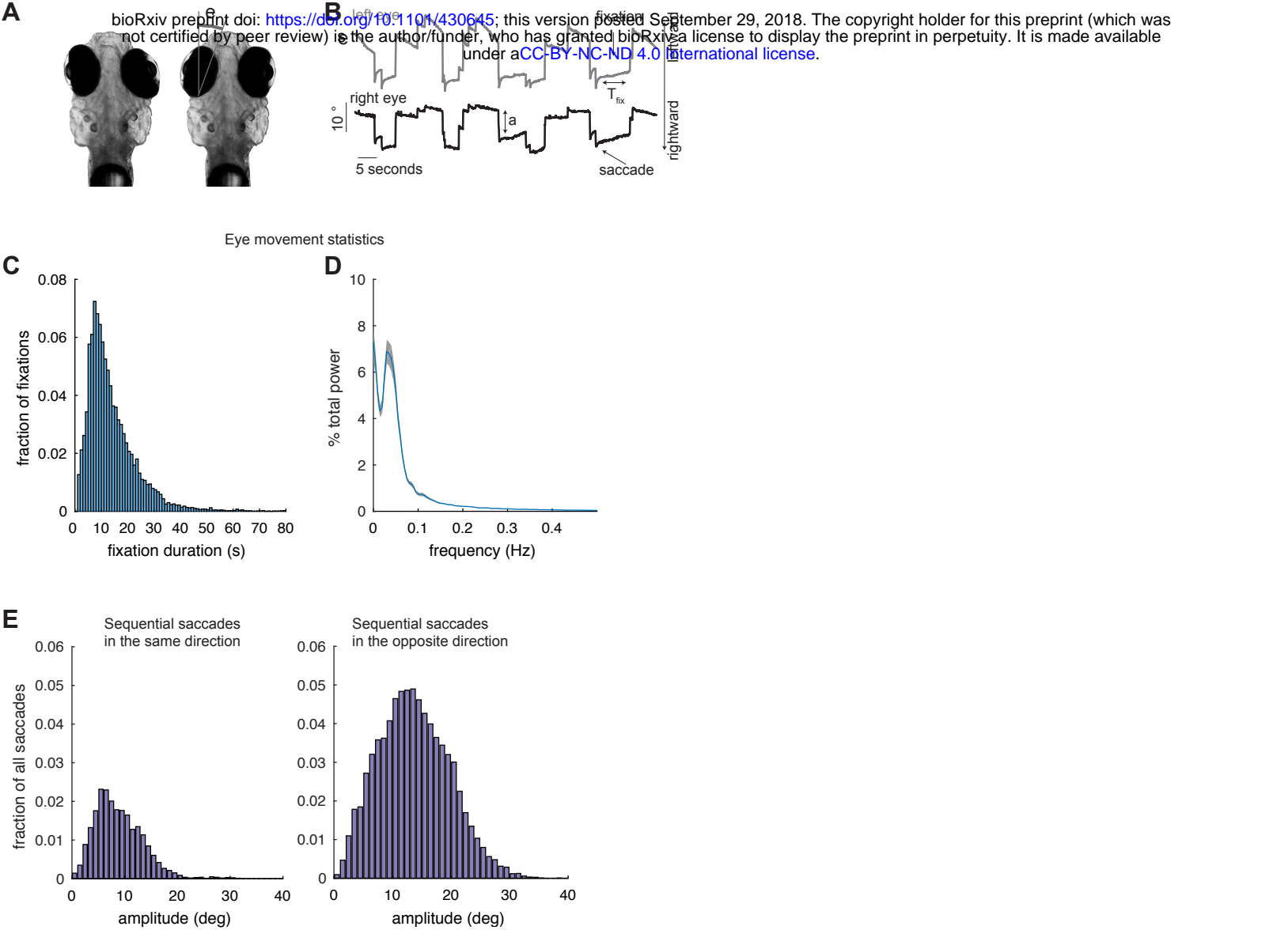


Figure 1

Figure 1. Spontaneous eye movements in larval zebrafish. (A) Changes in horizontal eye position, e , were recorded from agarose-restrained larval zebrafish while they made spontaneous eye movements in the dark. (B) Changes in horizontal eye position with time for both eyes. Saccade amplitude is denoted by a and fixation duration is denoted as T_{fix} . (C) Histogram of fixation durations measured across multiple animals ($n=16,033$ fixations from 20 fish). (D) Power spectral density (PSD) of eye-position changes as a function of frequency measured in Hertz and averaged across all fish used to construct panel C. Grey shading shows standard error about the mean. (E) Given two consecutive saccades, panels show histograms of the second saccade's amplitude (measured in degrees) for saccades made in the same direction (left column, $n=3,678$ saccades) or saccades made in opposite directions (right column, $n=12,355$ saccades).

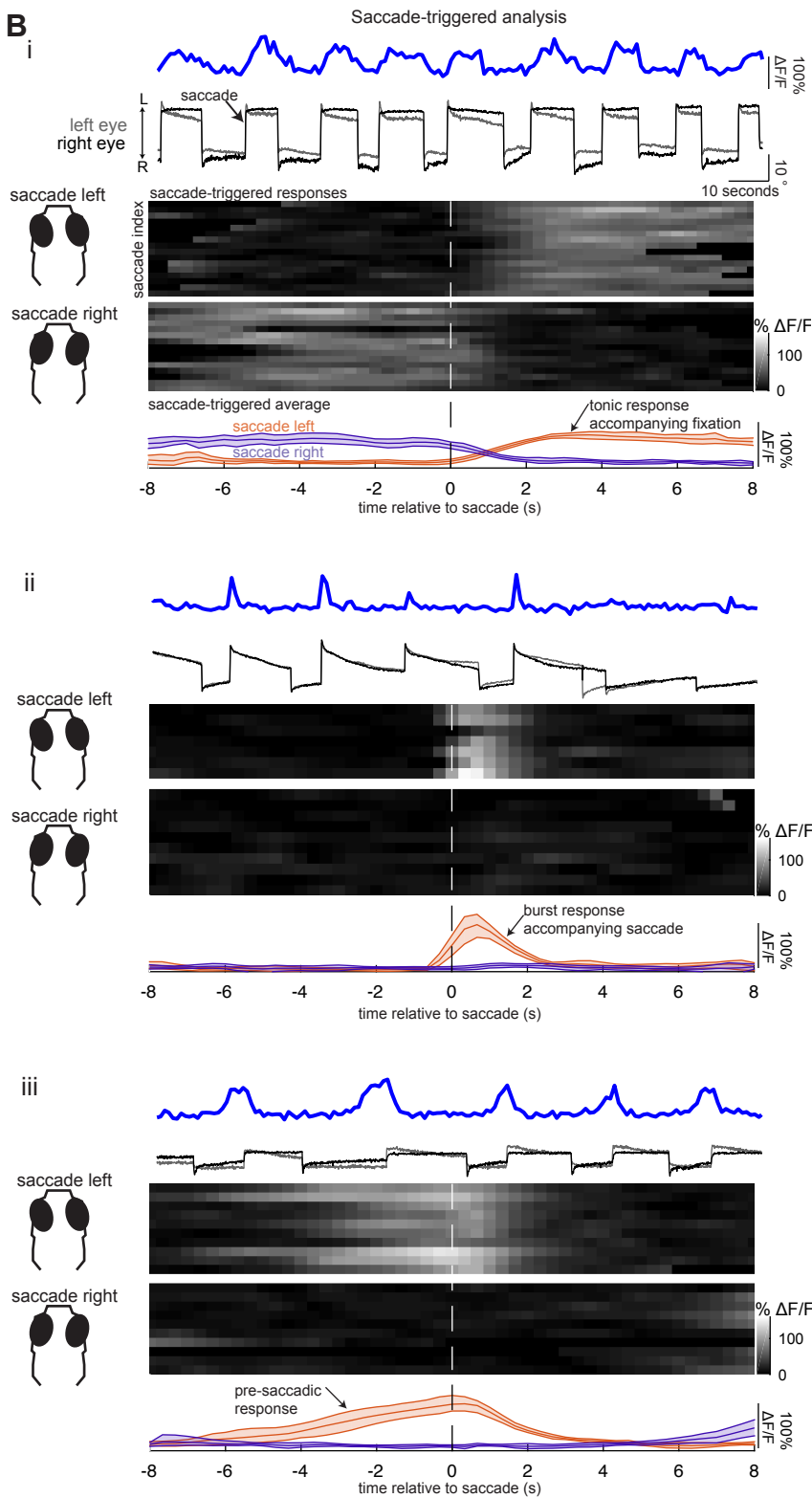
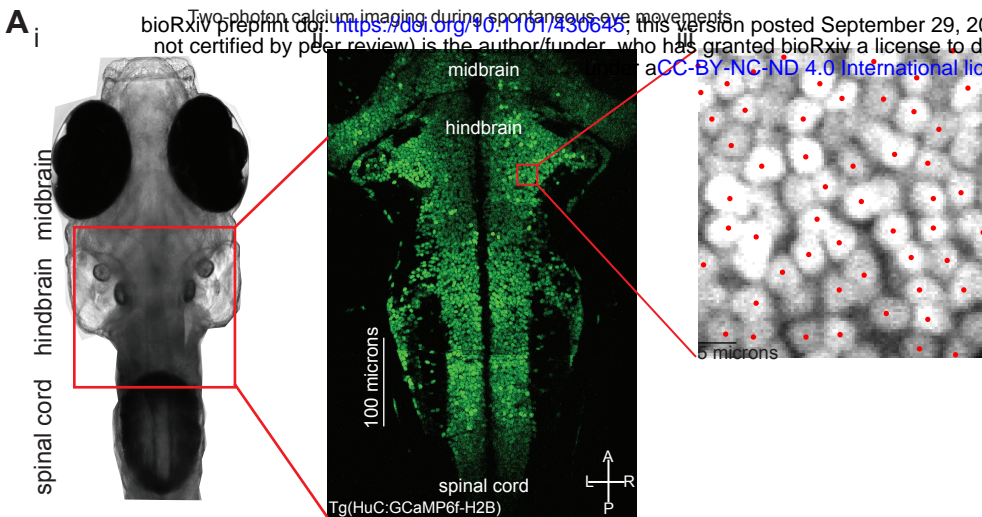


Figure 2

Figure 2. Two-photon calcium imaging during spontaneous eye movements. (A)(i) A 7-day old larval zebrafish. The hindbrain is outlined by the red box. (ii) Time-averaged calcium image showing all neurons within a single plane of the hindbrain. A, P, L, R denote anterior, posterior, left and right. (iii) Zoomed-in image of time-averaged nuclear-localized GCaMP6f expression showing typical resolution used. Red dots show the center-of-mass for automatically detected nuclei using standard computer vision algorithms (see methods). (B) Examples of simultaneously recorded eye movements and calcium activity along with saccade-triggered responses and averages. (i-iii, top row) Simultaneously recorded eye position and fluorescence trace (blue) created by averaging across all pixels within a single-cell. Leftward/rightward directed saccades are made toward the direction labelled L/R. (i-iii, middle row) Fluorescence trace is segregated into responses that occur before and after each saccade. Image of saccade-triggered responses around saccades to the left (upper middle) and saccades to the right (lower middle). Each row displays a saccade-triggered response. White dashed line shows time of saccade and grayscale color shows value of dF/F . Temporal axis shown in the bottom row. (i-iii, bottom row) Averages of saccade-triggered responses along with 95% confidence intervals. (i) Example of a cell with tonic post-saccadic activity. (ii) Example of a cell that displays a burst of activity triggered during the saccade. (iii) Example of a cell that displays pre-saccadic activity.

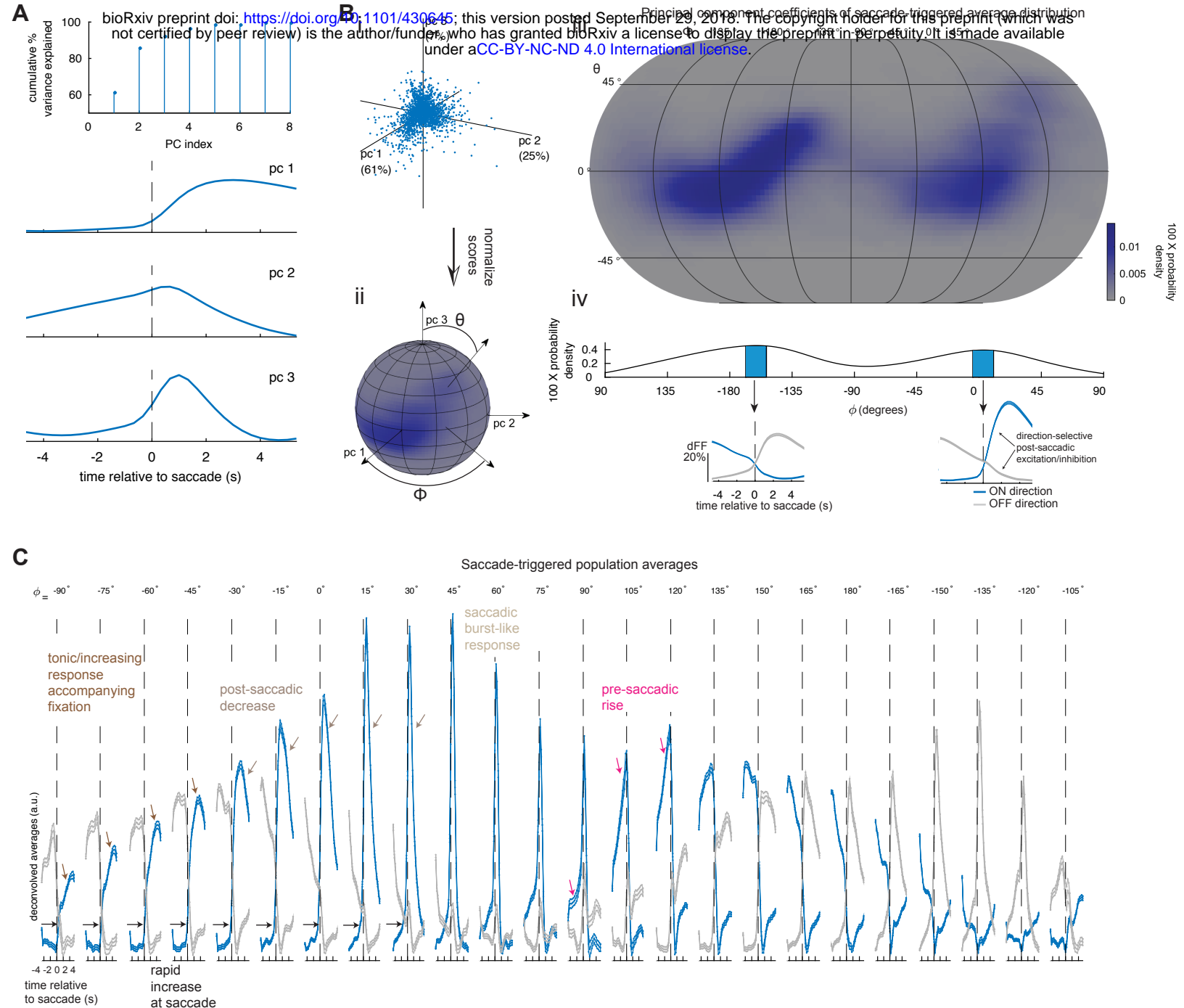


Figure 3

Figure 3. Averaging neuronal activity around time of saccade reveals a continuum of direction-selective calcium responses. (A) (Top row) Cumulative percent variance explained by each principal component. Other rows show the first three principal components of saccade-triggered average (STA) fluorescence responses sorted according to the amount of variance each one explains from most (component 1) to least (component 3). (B) (i) Scatter plot of principal component coefficients (scores) for the first three principal components. Each dot represents a different STA. (ii) The length of each score vector was normalized to 1 which allows each score to be described as a point on a sphere specified by longitude and latitude, ϕ and θ respectively. (iii) Two-dimensional (Eckert IV projection) probability density of the distribution of normalized scores. (iv) Probability density of normalized score longitudinal angle. The population average STA for responses corresponding to the most probable longitudinal angles (within 15 degrees; shaded blue region in density function) is shown in blue below the density function. The blue trace only reveals responses from one of each cell's two STAs. The population average responses around the other direction are shown by the gray trace. (C) Series of population-averaged STAs after deconvolving with an exponential kernel (2 seconds time constant). The population average shown in blue is comprised of STAs specified by the same value of ϕ (shown in the top row, up to 15 degrees). The population average shown in gray is comprised of the same cells but using the STA around the direction not used to make the blue trace.

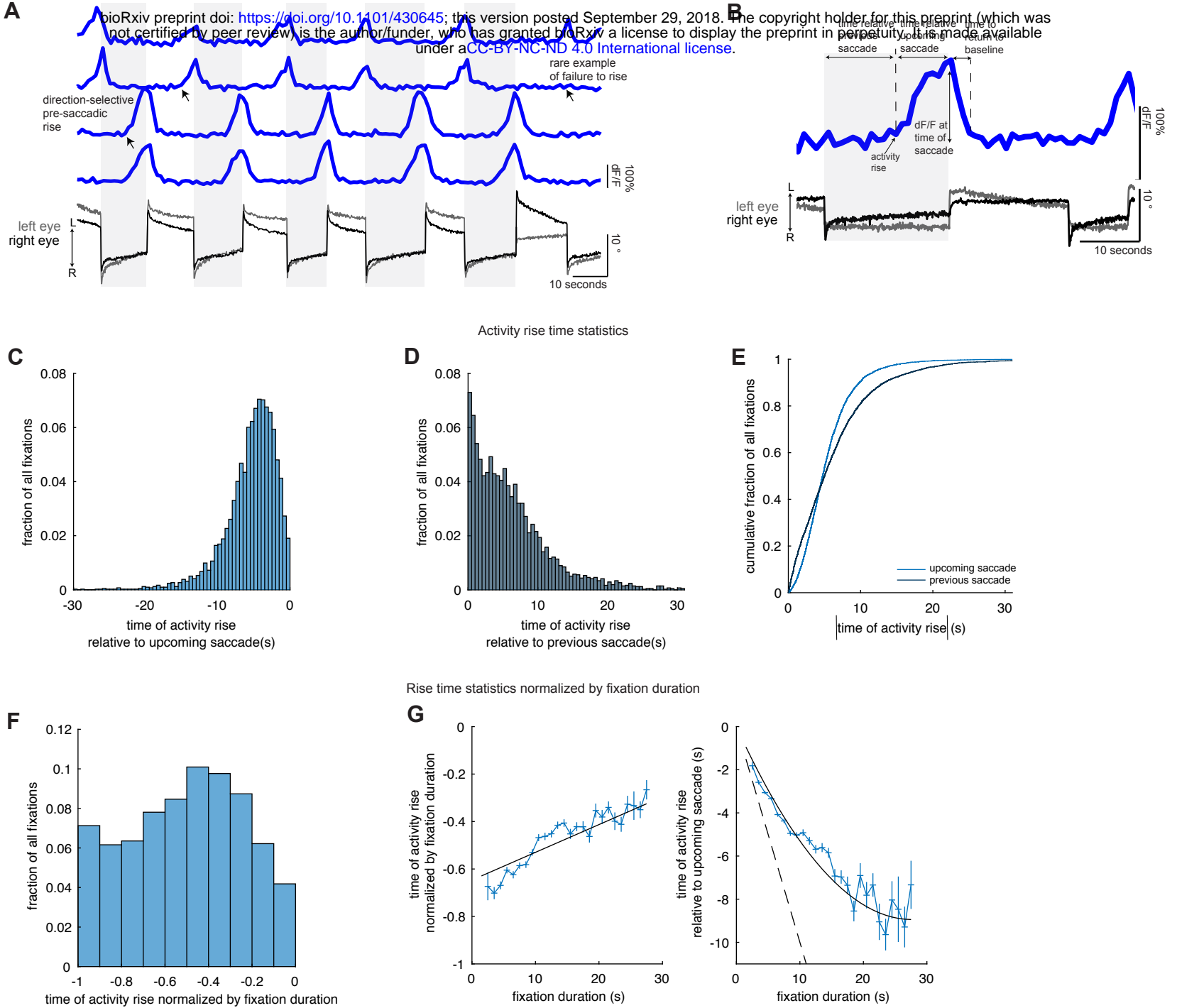


Figure 4

Figure 4. Neurons whose activity anticipates saccades in a direction-selective manner.

(A) Simultaneously recorded eye position (black and gray traces) and single-cell fluorescence responses (blue) from cells whose dF/F values rise before spontaneous saccades. Leftward/rightward directed saccades are made toward the direction labelled L/R in panels A and B. (B) Zoomed-in view of pre-saccadic fluorescence activity demonstrating the measurements of spontaneous pre-saccadic rise-time that were analyzed. (C) Histogram of times of pre-saccadic rise measured with respect to the time of upcoming saccade (n= 4,146 events from 20 fish). (D) Histogram of times of pre-saccadic rise measured with respect to the time of the previous saccade. Binsize in C and D is 0.5 seconds. (E) Comparison of the cumulative distribution function of spontaneous rise-time measured with respect to upcoming or previous saccade. Absolute value of the time of activity rise is plotted on the horizontal axis. (F) Histogram of times of pre-saccadic rise, measured with respect to upcoming saccade, normalized by fixation duration. (G) (left panel) Average time of pre-saccadic rise normalized by fixation duration as a function of fixation duration (blue). Line of best fit linear regression model shown in black. (right panel) Average time of pre-saccadic rise as a function of fixation duration. Slope of dashed line equals negative one. Solid black line shows the same linear regression model in the left panel multiplied by fixation duration. Error bars show standard error about the mean.

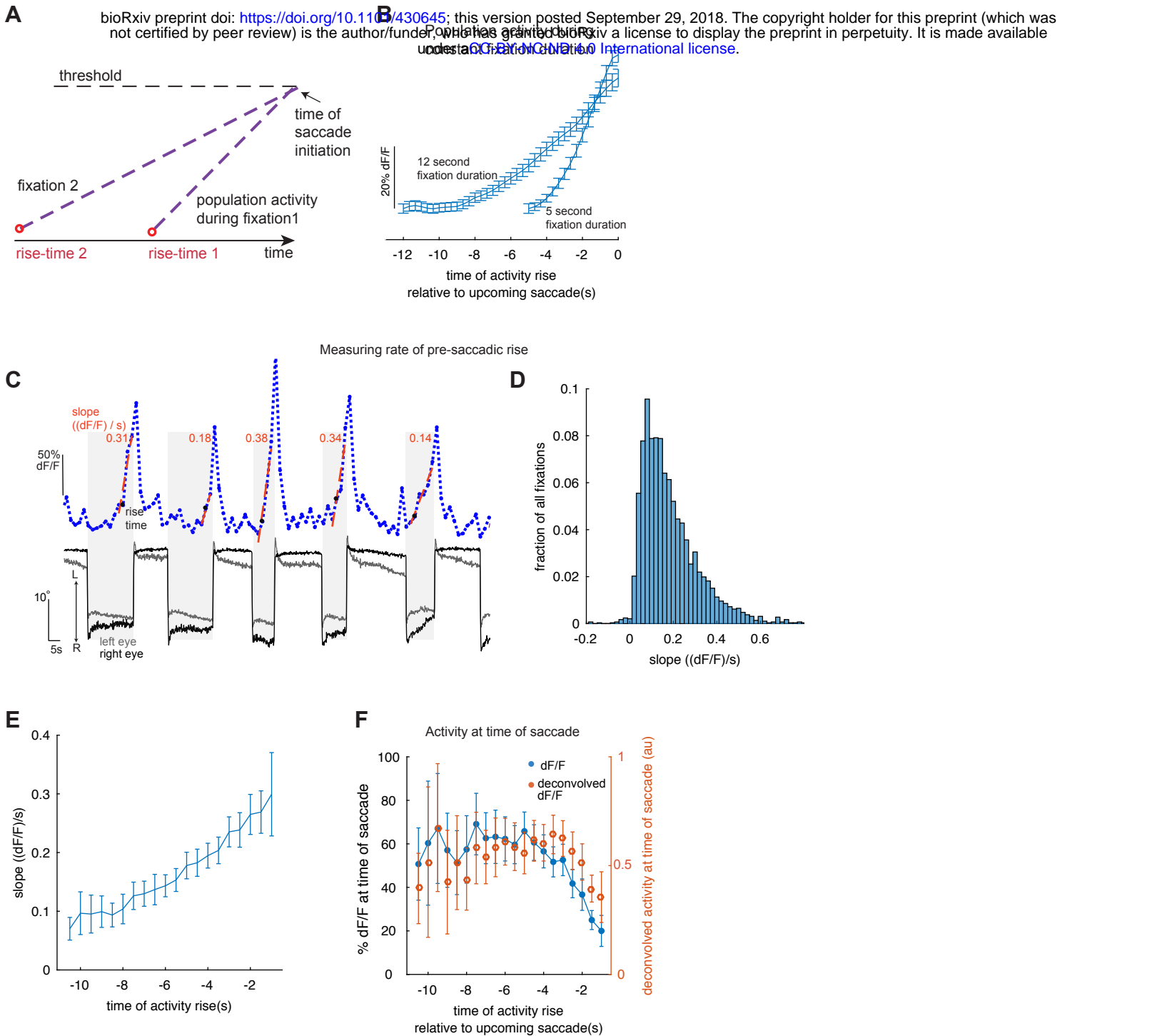


Figure 5

Figure 5. The rate and time of pre-saccadic rise vary in manner consistent with ramp-to-threshold models. (A) Hypothetical mechanism for how a pre-saccadic signal could initiate saccade. Activity from a population of neurons (purple dashed line) initiates saccades once it crosses an intrinsic threshold value (black dashed line). In fixation 1, activity rises (rise-time 1) earlier than in fixation 2 (rise-time 2). Since pre-saccadic activity in fixation 2 is assumed to reach the same threshold as pre-saccadic activity in fixation 1, activity in fixation 2 must rise more slowly than activity in fixation 1. (B) Population average pre-saccadic fluorescence as a function of time until upcoming saccade when fixation duration is held fixed to either 5 seconds (to within 0.5 seconds; $n=255$ fixations from 115 cells) or 12 seconds (to within 0.5 seconds; $n=177$ fixations from 148 cells). Fluorescence activity was interpolated at times evenly spaced by $1/3$ seconds. (C) Visualization of the slope statistic used to quantify rate of pre-saccadic rise before each saccade. Simultaneously recorded fluorescence activity (blue) and eye movements. Leftward/rightward directed saccades are made toward the direction labelled L/R. (D) Histogram of slopes of pre-saccadic fluorescence increases that are well fit by the linear model (correlation between best-fit line and data greater than 0.7, $n=2,922$ events). Binsize is 2 (dF/F)/s. (E) Average slope of pre-saccadic fluorescence increase as a function of time of pre-saccadic rise measured with respect to upcoming saccade. (F) Population average pre-saccadic fluorescence (blue dots) and deconvolved fluorescence (orange dots) at the time of saccade as a function of time of pre-saccadic rise measured with respect to upcoming saccade. The same fixations used to construct E are shown here. Error bars in B, E, and F show standard error about the mean.

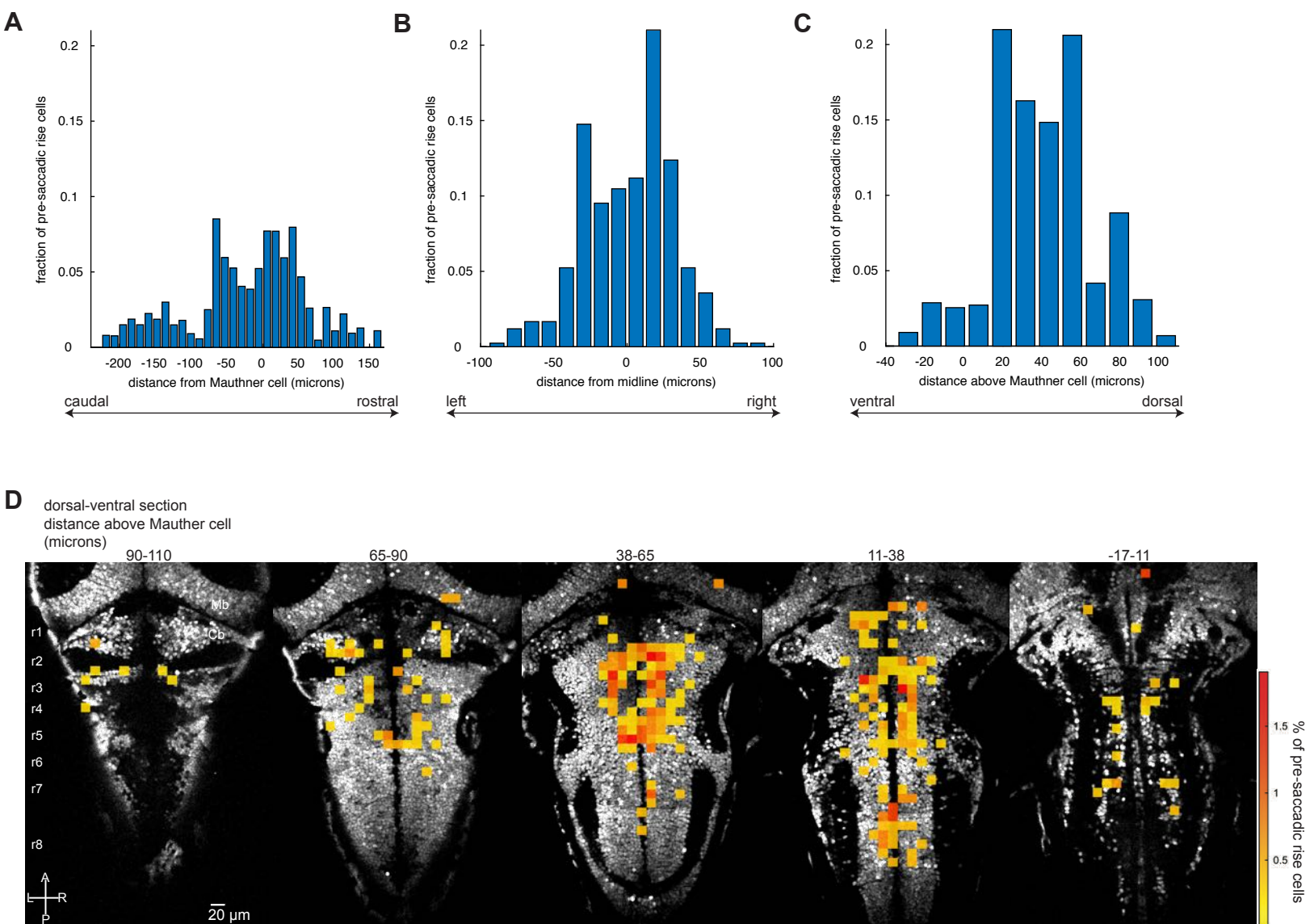


Figure 6

Figure 6. Spatial distribution of cells whose activity anticipates saccades. Histograms showing percentage of pre-saccadic neurons as a function of their registered location onto a common reference brain for the rostral-caudal (A), left-right (B), and dorsal-ventral (C) directions. Percentages are weighted to account for unequal numbers of fish used to sample different hindbrain regions. Binsize is 12 microns for all three panels. (D) Horizontal projections at fixed dorsal-ventral sections showing the percentage of pre-saccadic cells within 12x12 micron pixels, following alignment with a reference brain. Dorsal-ventral sections used range from most dorsal location where pre-saccadic cells were found (left panel) to most ventral location where pre-saccadic cells were found (right panel). Black and white background images show single planes from the reference brain. r1-8 indicates approximate rhombomere location within the reference brain. MB is midbrain. Cb is cerebellum. A, P, L, R denote anterior, posterior, left and right.

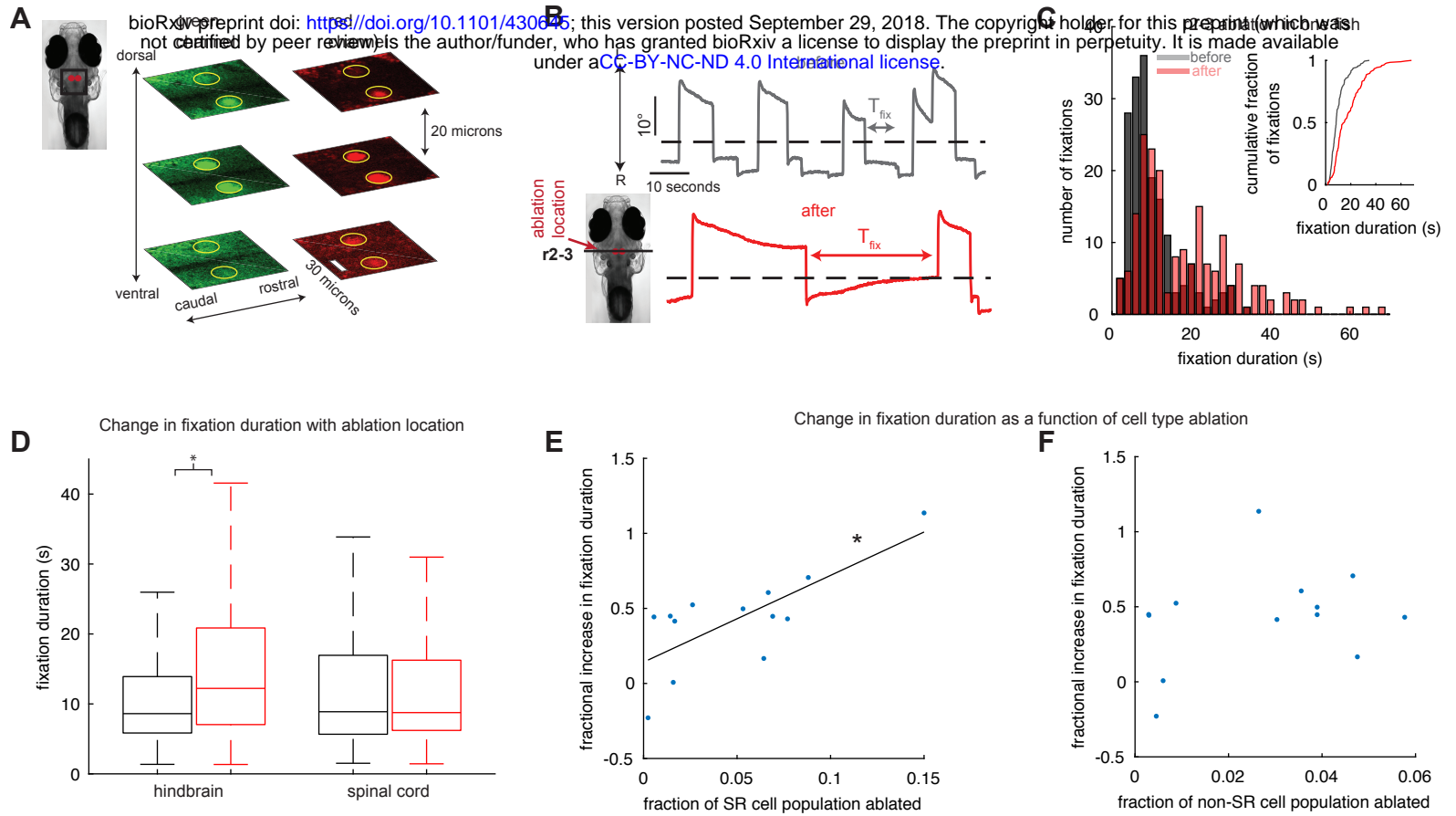


Figure 7

Figure 7. Focal laser ablations in regions containing pre-saccadic neurons result in increased fixation durations. (A) Time-averaged images showing horizontal sections taken from an individual fish following bilateral laser ablations. Each row shows sections from dorsal (top) to ventral (bottom) locations spaced apart by 20 microns. Ablated regions appear as bright, multi-spectrum fluorescent regions approximately 30 microns in diameter (highlighted in yellow). (B) Eye position versus time recorded before (gray) and after (red) ablations in the rostral hindbrain. r2-3 denotes rhombomeres 2-3; T_{fix} denotes fixation duration. Leftward/rightward directed saccades are made toward the direction labelled L/R. Only changes to the left eye are shown for demonstration purposes. (C) Histogram of fixation durations measured in both eyes before (gray) and after (red) ablations for the animal shown in (B). Inset shows a cumulative distribution plot of the same data. (D) Boxplot of fixation durations measured in both eyes before (gray) and after (red) ablations grouped according to ablation location. Central mark shows the median, edges of the box are the 25th and 75th percentiles, and whiskers show the range of values. Stars show significant differences. (E) Average fractional increase in fixation duration as a function of estimated fraction SR cell population ablated (blue dots). Solid black shows best-fit regression line. Fractional increase in (E) and (F) is measured as median duration after ablation divided by median duration before ablation minus one. (F) Average fractional increase in fixation duration as a function of estimated fraction of eye movement-related cells ablated that do not have pre-saccadic activity.

Supplemental Experimental Procedures

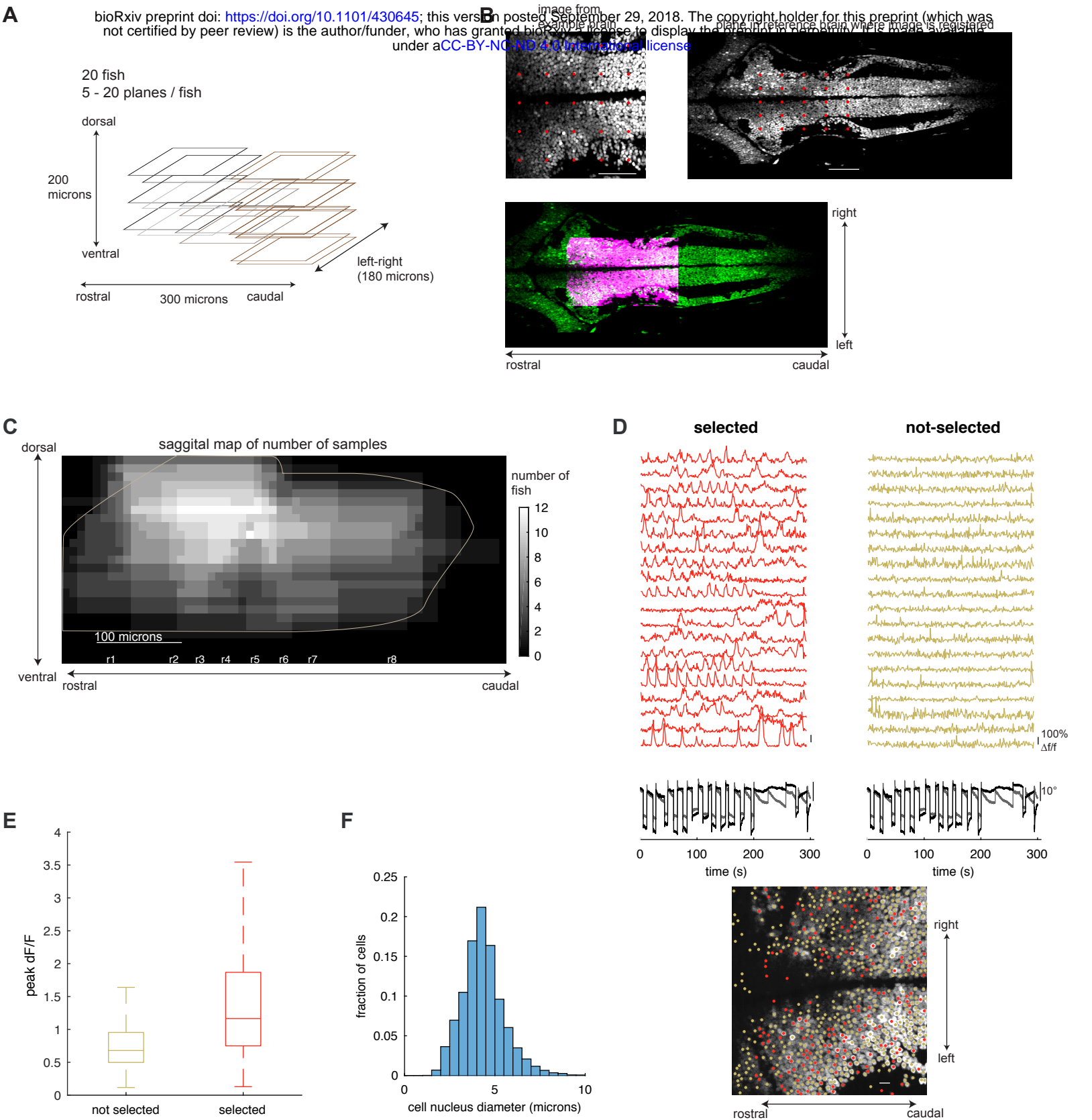
Pre-Processing of Calcium Movies

We first calculated the median fluorescence intensity across time for each pixel in the movie and used the resulting image as a reference. Any frame in the movie that deviated from the reference image was considered to have a movement artifact which required correction. To register each movie frame to the reference, we used the Matlab function *dftregistration* which implemented the two-step discrete Fourier transform (DFT) algorithm described in (Guizar-Sicairos et al., 2008). For computational efficiency the *dftregistration* algorithm worked in Fourier space to calculate cross-correlations. We used Matlab's built-in fast Fourier transform software (*fft2*) to compute each frame's two-dimensional DFT and to compute the two-dimensional DFT of the reference frame. Briefly, the *dftregistration* algorithm estimated the peak in the two-dimensional cross-correlation between the reference image and movie frame being registered. Each movie frame was then translated by an amount determined from the peak location. If the value of peak cross-correlation was too low, the frame was considered too aberrant to be useful and the fluorescence of all pixels in this frame were replaced by NaNs. Specifically, for each frame, the *dftregistration* algorithm returned an error value related to the square root of one minus peak, normalized cross-correlation between a given frame and the reference. For each imaging plane, we computed the median error across all frames and the median absolute deviation (MAD) of the error across all frames. If a given frame's error value was greater than 5 times the MAD plus the median that frame's pixels were replaced by NaNs.

CalAn-MATLAB Routines Used to Find the Locations of all Cell Nuclei Based on Fluorescence Dynamics

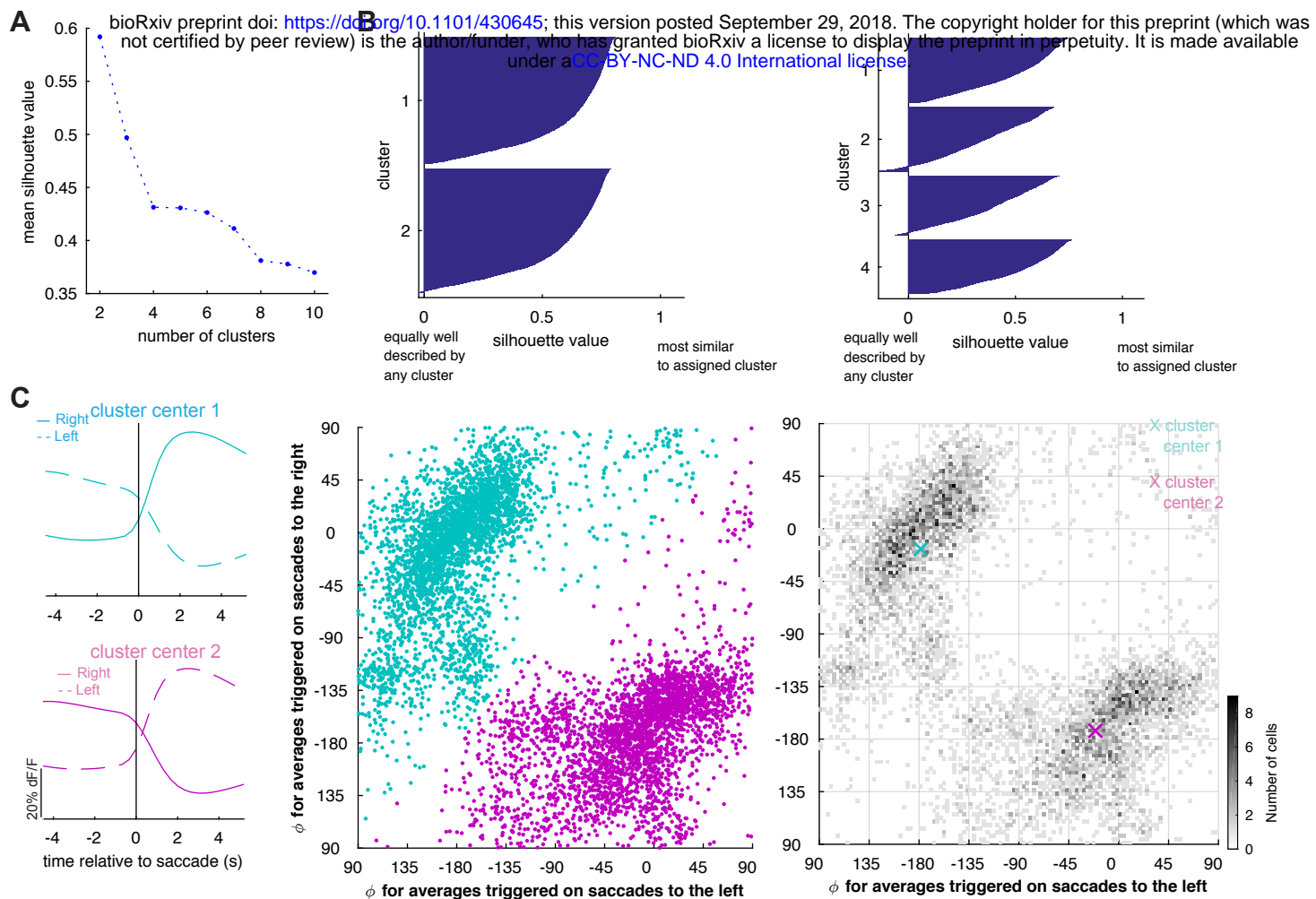
We first found initial estimates for the spatial, temporal and background components using the *initialize_components* function. This function ran several steps: 1) it spatially filtered the fluorescence movies (Gaussian kernel with standard deviation set to 5, which corresponds to 1.8 microns). 2) it greedily selected locations where the spatial estimates explained the largest amount of spatio-temporal variance. 3) it used rank-1, non-negative matrix factorization to produce spatial, temporal, and background estimates. 4) it refined these estimates using a

hierarchical, alternating, non-negative matrix factorization method. 5) it ran a rank 1 non-negative matrix factorization on the spatio-temporal residual to initialize the background spatial and temporal components. We updated the initial estimates of the spatial footprints and the background component using the constrained non-negative Lasso algorithm implemented in the *update_spatial_components* function. We used the 'dilate' option which computed the search location by dilating the support set of each component from the previous iteration using a 4-pixel radius (1.4 microns) disk-shaped structuring element. The new components are then post-processed by the following operations: (i) 2-d median filtering with a default size of 3x3 pixels (ii) morphological closing with a length 3 pixel, square shaped structuring element, and (iii) energy thresholding with threshold set to 0.99. We then updated the estimates of the temporal components using the *update_temporal_components* function with an auto-regressive parameter, p , equal to zero. This function updated components using a block-coordinate descent algorithm (we used 2 iterations) which, with p equal to zero, ran a thresholding operation (at a threshold of 0) on the activity of each component after removing the effect of all the other components. After one spatial and temporal update, we removed spatial or temporal components that were poorly correlated with the raw data (space and time r -values returned by *classify_comp_corr* function were less than 0.05) or whose spatial footprints were larger than a threshold (16 pixels which equaled 5.8 microns). We then merged spatially overlapping components with highly correlated temporal activity ($cc > 0.95$) using the *merge_components* function. Using the new component estimates we then ran one more iteration of the spatial and temporal component updates described above. Finally, since we were only interested in the spatial locations of active neurons, we set non-zero values for each spatial component to one and estimated each component's neuronal activity as the trace that resulted from spatially-averaging fluorescence at non-zero locations.

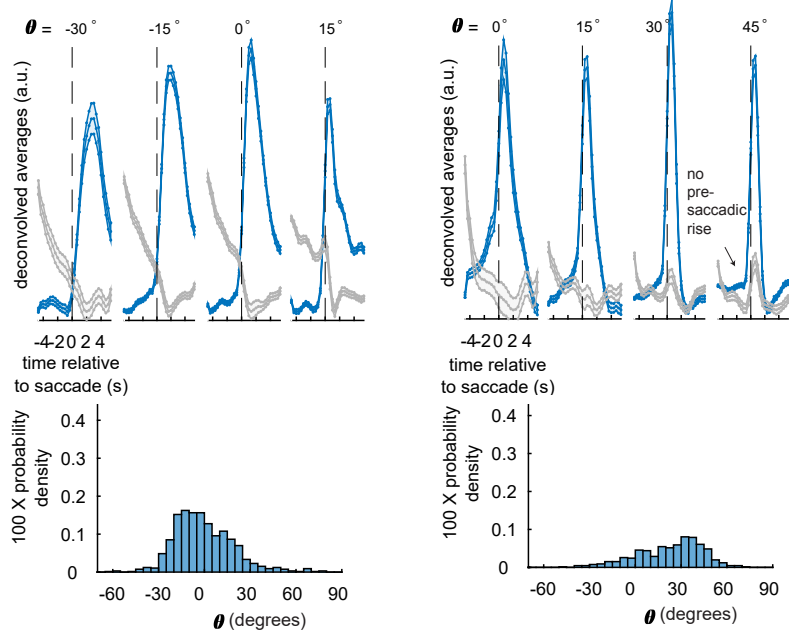


Supplemental Figure 1

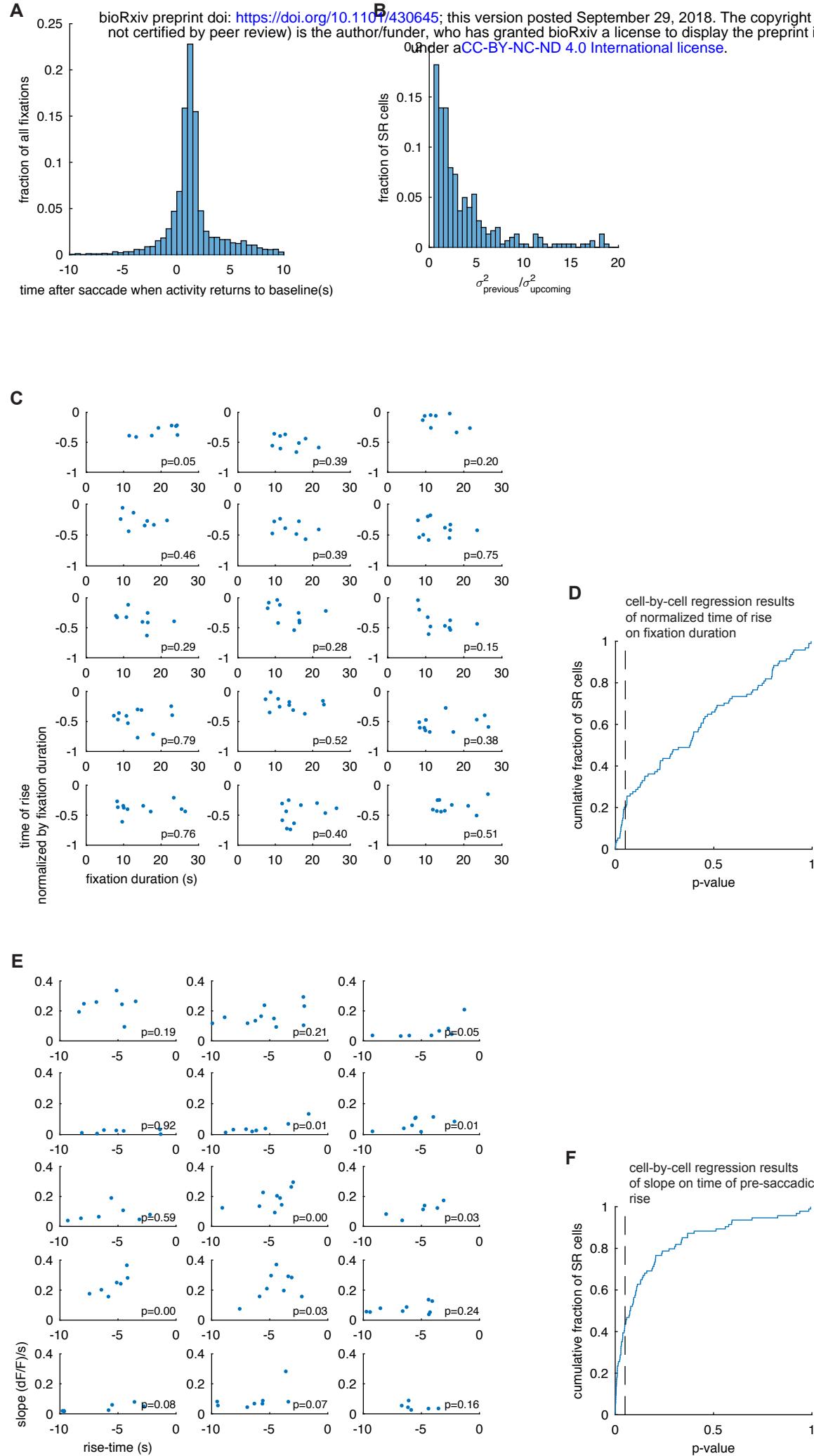
Supplemental Figure 1. Methods used for imaging and analyzing cells across the hindbrain. (A) Cartoon schematic of sampling method used. Each square represents a horizontal imaging plane. A single imaging plane had a side-length of 185 microns and did not cover the entire rostral-caudal extent of the hindbrain. Overlapping segments of the hindbrain were imaged in multiple fish (different colors) and then registered to a reference brain resulting in hindbrain-wide imaging across the population. (B) (top, left panel) Time-averaged calcium image showing all neurons expressing GCaMP6f within a single example imaging plane. (top, right panel) Time-averaged calcium image of the plane within the reference hindbrain where the example was registered. Red dots show control points used in constructing the registration transformation. (bottom panel) Example image after registration (pink) laid over the reference brain (green). Scale bar length is 50 microns. (C) Panel shows a heat map of the number of animals used to sample each location from a sagittal view (20 fish in total). Each voxel in the reference brain was sampled using at least 3 different animals. (D) Segregating active versus non-active neurons. Example traces of dF/F versus recording time from cells imaged in the same plane (cell locations shown by color-coded dots in image at the bottom; scale bar length is 10 microns). Beneath dF/F traces we plot accompanying eye movements. Cells in the right column were detected based on morphology but were not classified as active by the NMF algorithm. These cells generally have smaller fluctuations in dF/F than cells in the left column that were selected by the NMF algorithm based on activity. (E) Boxplot of maximum dF/F value across time from a population of cells selected by the NMF algorithm (selected) and cells labelled as background by the algorithm (not-selected). Central bar shows the median, edges of the box are the 25th and 75th percentiles, whiskers show the range of values. We rejected the null hypothesis that the average peak dF/F values are equal for the two populations ($p < 0.01$, one-way ANOVA; $n = 216,717$ non-selected cells, $n = 64,242$ selected cells). (F) The area of the spatial footprint found by the NMF algorithm (see methods) yields a measurement of nuclei area and diameter. Panel shows a histogram cell nuclei diameters across all 216,717 detected regions-of-interest.



Supplemental Figure 2. Analysis of combined left and right saccade-triggered averages across the population. K-means was used to cluster the normalized principal component coefficients (see Fig. 3). Only the coefficients corresponding to the first three principal components were used in the analysis. For each cell, the 3 coefficients characterizing saccade-triggered averages (STAs) triggered to left and the 3 characterizing STAs to the right were combined to create a 6-dimensional vector. K-means was run using 2-10 clusters. (A) A Silhouette analysis was performed on the output of each run to evaluate the quality of clustering. The largest average silhouette value (best clustering) is achieved using 2 clusters. (B) Silhouette plot of the K-means results using 2 clusters (left panel) and 4 clusters. (C) Scatter plot and two-dimensional distribution of normalized score values of phi (see longitudinal angle in the globe in Fig. 3B) for STAs to the right versus left. Dots in the scatter plot are colored according to their assigned cluster after running a K-means analysis on the plot with K=2. Binsize used to construct the two-dimensional distribution plot is 1 degree. The far left panels show examples of STAs to the left (dashed) and right (solid) created by combining first three principal components weighted by coefficients corresponding to the first (top, left) or second (bottom, left) cluster center. The center of cluster 1 corresponds to STA pairs that increase in value following saccades to the right and decrease in value following saccades to the left. The center of cluster 2 shows similar activity but with the opposite directional preference.

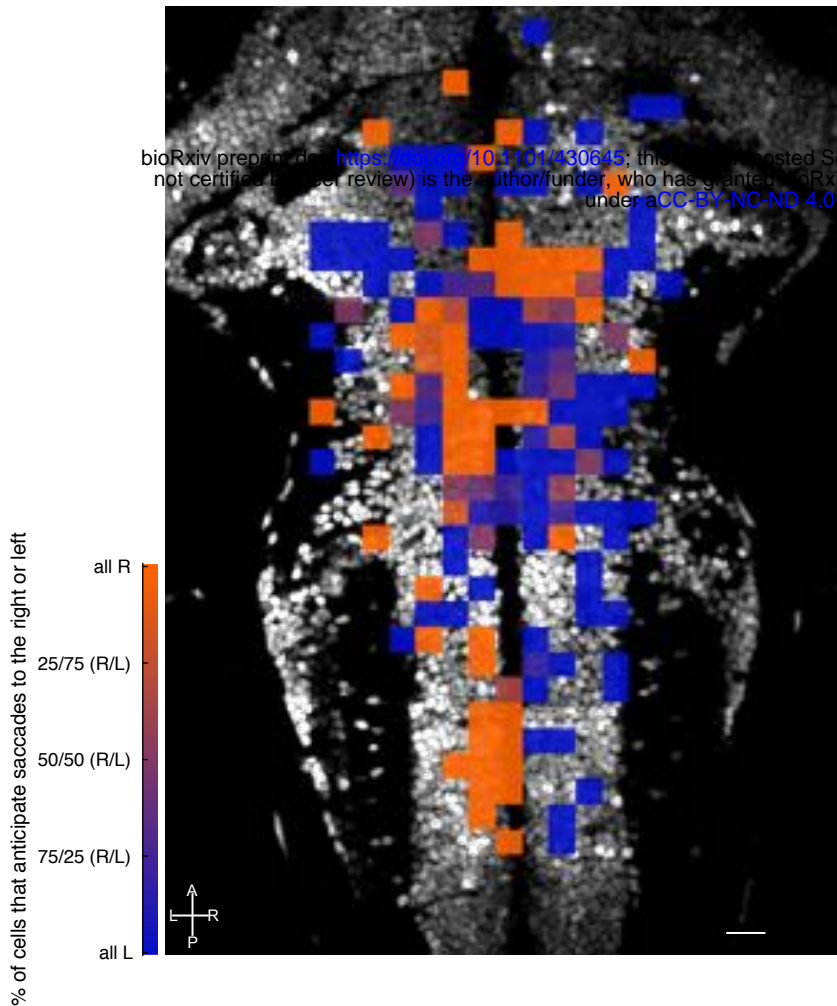


Supplemental Figure 3. Qualitative features of saccade-triggered averages do not vary with latitude value of normalized principal component coefficient. (Top row) Saccade-triggered fluorescence responses averaged across cells after deconvolving with an exponential kernel (2 seconds time constant). Each column shows a different population average from responses with distinct normalized principal component coefficients (see the globe in Fig. 3B for the angular representation of normalized principal component coefficients). The population average shown in blue is comprised of saccade-triggered averages specified by the same value of longitudinal angle ϕ (either 0 or 45, within 15 degrees) and angle of latitude, θ , (shown in the top row, within 15 degrees). The population average shown in gray is comprised of the same cells but using the saccade-triggered average around the direction not used to make the blue trace. (Bottom row) Histograms of latitude for all saccade-triggered averages with a longitude value of either 0 (bottom, left) or 45 (bottom, right). The population averages shown in Figure 3C average together the variation across latitude shown here. We only show variations across latitude for groups with longitude fixed to 0 or 45 degrees because these groups displayed the largest variation across latitude. In most cases, the averages shown in Figure 3C capture the qualitative features of cell populations that have been sub-grouped by latitude.



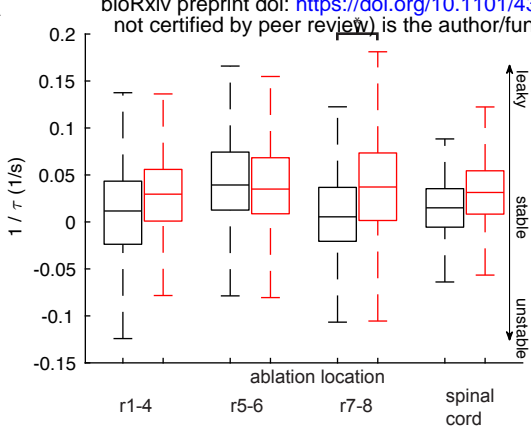
Supplemental Figure 4. Population and single-cell analysis of pre-saccadic rise features.

(A) For each SR cell we measured the time when the non-negative, deconvolved approximation to cell firing rate returned to baseline after rise events. Histogram of the time when pre-saccadic rise activity returns to baseline across the population ($n = 4,146$ events from 20 fish). (B) For each SR cell we measured the variance across saccades in the time of rise relative to the previous saccade, $\sigma^2_{\text{previous}}$, and the variance across saccades in the time of rise relative to the upcoming saccade, $\sigma^2_{\text{upcoming}}$. Histogram across cells of the ratio of variances in time of rise (median ratio = 1.9; $n = 373$ cells). Each cell was required to be measured with greater than 5 simultaneously recorded saccades. (C) Scatter plots of time of pre-saccadic rise normalized by fixation duration relative to upcoming saccade as a function of fixation duration for 15 example cells. Each sub-plot corresponds to a different cell. For each cell, we quantified the relationship between the plotted statistics using a simple linear regression of normalized fixation duration on fixation duration. The number at the bottom of each plot reports the p-value for the t statistic obtained under the null hypothesis that the slope regression coefficient is zero. (D) Cumulative distribution of the p-values reported in (C) for all 94/420 pre-saccadic rise cells in the population. We only use cells that have at least 8 saccades and a wide enough spread in fixation durations to be useable (inter-quartile range in fixation durations greater than or equal to 5 seconds). Only 20 percent of single cells had a significant p-value (less than 0.05, dashed line) and only 17 percent had a significant p-value and had the same trend (positive slope) as the population. (E) Scatter plots of slopes of pre-saccadic fluorescence increases that are well fit by a linear model (see Fig. 5 and accompanying text) as a function of time of pre-saccadic rise for 15 randomly chosen example cells. Each sub-plot corresponds to a different cell (panels in (C) do not necessarily correspond to panels in (E)). For each cell, we quantified the relationship between the plotted statistics using a simple linear regression of slope on time of pre-saccadic rise. The number at the bottom of each plot reports the p-value for the t statistic obtained under the null hypothesis that the slope regression coefficient is zero. (F) Cumulative distribution of the p-values reported in (E) for all 94/420 cells in the population that have at least one pre-saccadic rise event that is well-fit by a linear function of time (cc between rising fluorescence data and model is greater than or equal to 0.7) and that have enough samples and a wide enough spread in fixation durations to be useable (at least 8 saccades and an inter-quartile range in fixation durations greater than or equal to 5 seconds). 44 percent of the cells in the plot have a significant p-value ($p < 0.05$, dashed line) and have the same trend (positive slope) as the population.

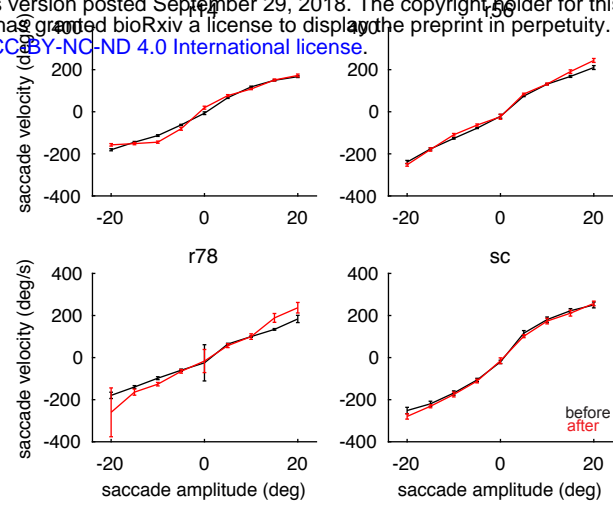


Supplemental Figure 5. Directional preference of pre-saccadic rise cells. Horizontal projection of directional preference for all pre-saccadic rise cells following alignment with a reference brain. Black and white background image shows one plane from the reference brain for visualization purposes. The color of each 12x12 micron pixel denotes an average of how many cells registered to that square have activity that rises before saccades to the left (blue) or to the right (orange). Squares with violet colors in-between blue and orange indicate that cells with both left and right preference were registered to that location. Scale bar length is 20 microns. A, P, L, R denote anterior, posterior, left and right.

A

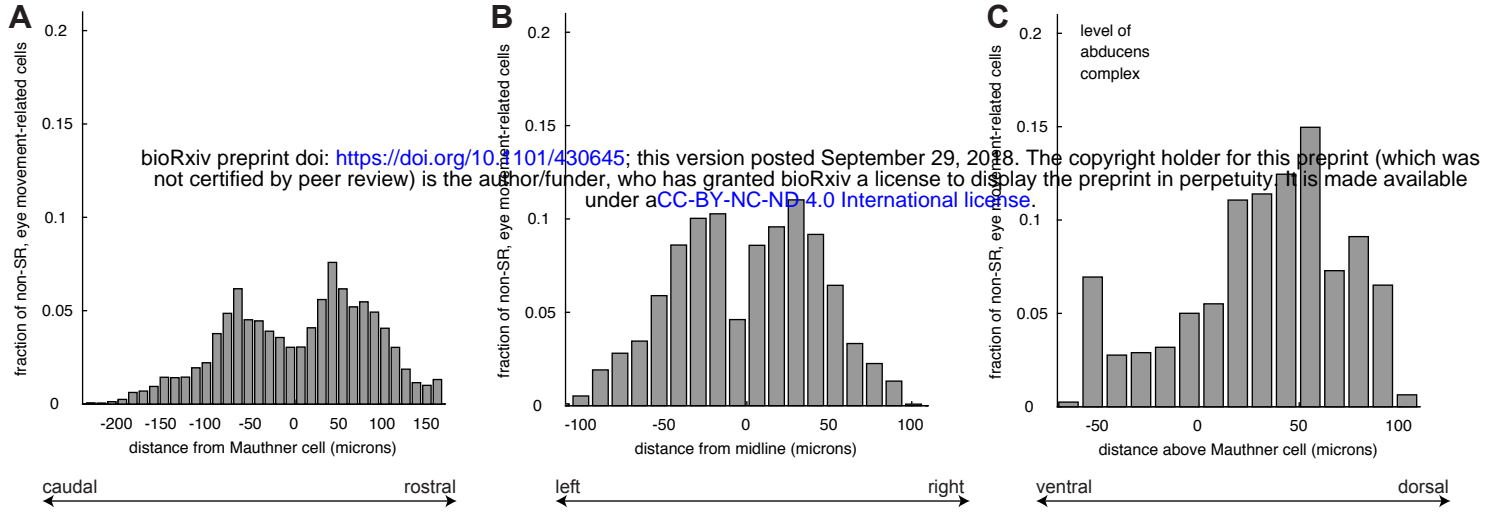


B



Supplemental Figure 6. Changes in saccade velocity and rate of eye position decay

following ablation. (A) The rate of eye position decay following saccades was measured using an exponential function with time constant τ . Boxplot of inverse τ values before (gray) and after (red) ablations grouped according to ablation location. Large positive values of $1/\tau$ correspond to events where the eyes rapidly returned to nasal resting position. Negative values of $1/\tau$ correspond to events where the eyes continued to move away from nasal resting position after saccade. Central mark shows the median, edges of the box are the 25th and 75th percentiles, whiskers show the range of values. Stars show significant differences ($p < 0.001$, two-sample t-tests using Bonferroni correction to control for familywise error rate; $n = 5,676$ fixations before and 1,335 fixations after for rhombomeres 1-4 (r1-4), $n = 2,038$ fixations after for rhombomeres 5-6 (r5-6), $n = 2,653$ fixations after for rhombomeres 7-8 (r7-8), $n = 1,188$ fixations after for spinal cord). (B) Average saccade velocity, grouped according to ablation location, before (gray) and after (red) ablations as a function of saccade amplitude. $n = 2,060$ saccades before and 1,339 saccades after for rhombomeres 1-4, $n = 1,510$ saccades before and 2,038 saccades after for rhombomeres 5-6, $n = 4,972$ saccades before and $n = 2,661$ saccades after for rhombomeres 7-8, $n = 896$ saccades before and $n = 1,192$ saccades after for spinal cord ablations. Error bars show standard error about the mean.



Supplemental Figure 7. Distribution of cells with eye movement-related activity that do not have pre-saccadic ramping activity. Histograms showing percentage of eye movement-related neurons that do not have pre-saccadic ramping as a function of their registered location onto a common reference brain for the rostral-caudal (A), lateral-medial (B), and dorsal-ventral (C) directions. Percentages are weighted to account for unequal numbers of fish used to sample different hindbrain regions. Binsize is 12 microns for all three panels.